Aerosol distribution in the northern Gulf of Guinea: local anthropogenic sources, long-range transport and the role of coastal shallow circulations

By C. Flamant et al.

Reply to the referees' comments

In the following, the comments made by the referees appear in black, while our replies are in red, and the proposed modified text in the typescript is in blue.

Referee #1 comments

General Comments

This paper analyzes aircraft observations of aerosols collected along the coast of South West Africa during the DACCIWA field campaign in June-July 2016. The authors go on to speciate the observed aerosol types and identify the likely aerosol emission sources and atmospheric dynamics that led to their transport and eventual spatial distribution recorded during the case study. The paper is well-written, well within the scope of ACP, and it is refreshing to see an observational study from this region, which has historically been observationally-sparse, making it a new addition to the scientific literature. Overall, it is easy to follow the narrative and methodology of the paper, although there are a few places that may need clarification or further explanation, which are mentioned below.

We would like to thank the reviewer for his/her mindful and benevolent comments on the paper. We have worked hard to comply with all of them. We now also acknowledge the work of the anonymous referee in the acknowledgement section of the paper.

It would be nice to see a description on why this day of the field campaign was chosen for analysis. It seems like there is two months' worth of data from this project, so what makes 02-July-2016 so unique that it warrants its own paper, and how representative is it of typical flow patterns for this regime in the region?

The flight made in the afternoon of 2 July is unique in the sense that it is the only flight conducted over the ocean during which the downward looking lidar ULICE was operational. The combination of remote sensing to monitor the aerosol landscape over the Gulf of Guinea and in situ measurements to assess the nature of the observed aerosols was only possible on that day. For information, two other so-called OLACTA flights were conducted with the ATR 42 during the campaign. However, the lidar was not working and only in situ, low-level measurements were made.

We have added this bit of information in the Introduction, at the end of the penultimate paragraph as:
"The flight made in the afternoon of 2 July is unique in the sense that it is the only flight conducted over the ocean during which a downward looking lidar was operational. The combination of remote sensing to monitor the aerosol landscape over the Gulf of Guinea and in situ measurements to assess the nature of the observed aerosols was only possible on that day."

The primary concerns raised in the specific comments section regard aerosol aging and water uptake in humid environments, and timing of tracer release and the interpretation of maximum aerosol extent in the model.

We have hopefully clarified these issues in the following.

It is recommended that the manuscript be published in ACP after the specific and technical comments are addressed in the paper.

Specific Comments

Page 2 - Lines 32-34) States that the lower troposphere aerosol loading includes emissions from Lagos, but later in the paper the tracer experiment shows that the aerosol plumes over the ocean do not have a signal from Lagos. Is this a reference to Lagos being an aerosol source in the SWA region, instead of the over the limited ocean aircraft data from this case study?

Absolutely. Lagos is a large source of anthropogenic emissions in SWA. However in the domain of operation of the aircraft, which is quite far west compared to Lagos, and given the general direction of the monsoon flow, emissions from Lagos did not impact air quality in the region of interest for the present study.

We have modified the sentence in lines 41-42 (abstract) and lines 814-816 (conclusion) to clarify this in the revised manuscript.

In the abstract:
"*Given the general direction of the monsoon flow, the tracer experiments indicate no contribution from Lagos emissions to the atmospheric composition of the area west of Cotonou, where our airborne observations were gathered*."

In the conclusion:
"[…] given the general direction of the monsoon flow, Lagos emissions (taken to be 13 times that of Cotonou) do not appear to have affected the atmospheric composition west of Cotonou, where our airborne observations were gathered, as also shown by Deroubaix et al. (2018) in the summer in post-monsoon onset conditions, […]"

Page 4 - Lines 81-84) Is the purpose of DACCIWA / this paper to understand how atmospheric dynamics influences aerosol emission rates (e.g. stronger surface winds will loft more dust), or only aerosol transport after emission, or both?

The purpose of DACCIWA is to understand aerosol transport after emission.

The sentence was modified in the revised manuscript to include this information:
"One of the aims of the EU-funded project Dynamics-Aerosol-Chemistry-Cloud Interactions in West Africa (DACCIWA, Knippertz et al., 2015b) is to understand the influence of atmospheric dynamics on the spatial distribution of both anthropogenic and natural aerosols over SWA after emission."

Page 7 - Lines 161-163) Even though the optical properties could not be retrieved with the ULICE lidar inversion procedures, they were retrieved using other instrumentation, correct? If not, what was excluded?

Yes, the optical properties could be retrieved with other instrumentation described in the subsequent sub-section (section 2.1.2), namely a Particle Soot Absorption Photometer, a CAPS-PMex, and an integrated nephelometer (Ecotech, model Aurora 3000).

Pages 7-8 - Lines 178-186) Can sea salt be identified with this method?

No, the selected gas phase chemistry and aerosol metrics selected are only intended to discriminate between biomass burning aerosols associated with long-range transport from the south, anthropogenic pollution and dust particles associated with long-range transport from the north. In order to formally identify sea-salt we would need to include filter analysis, which were not conducted at this point. Nevertheless, sea salt particles can be identified from the lidar measurements as being associated with high backscatter and low depolarization (as discussed in the paper) as well as reflected in the large particles concentration ($N_{PM2.5}$) measured over the ocean and inland. However, from this we are not able to segregate sea-salt from other aerosols in case of mixture in the ABL.

A sentence was added in Section 2.1.2 in the revised manuscript, after the description of the metrics:
"Sea salt cannot formally be identified with the in situ measurements conducted with the ATR 42 payload during DACCIWA."

Pages 7-8 - Lines 178-186) What happens when there is a mixture of aerosol species instead of homogeneous plumes? Looking at Figure 10-b, the CALIOP data suggests a heterogeneous aerosol air mass during this case study event (e.g. dust mixing with smoke).

We agree that homogeneous plumes for a given aerosol type will likely only be observed fairly close to the sources, and that in the broader area of the aircraft operation, mixing is likely to occur. Rather than indicating homogeneous plumes, our metrics are an indication of what type of aerosol dominates the composition of a given sampled air mass. This is now more clearly stated in the revised manuscript.

A couple of sentences were added at the end of the 1st paragraph of Section 2.1.2 in the revised manuscript:
"Because of the complex atmospheric dynamics in the area, we cannot assume that only homogeneous air masses will be sampled with the aircraft. Rather, the selected observations are indicators of which type of aerosol dominates the composition of a given sampled air mass."

Pages 7-8 - Lines 178-186) Because the aircraft measurements were taken over the ocean, the particles reside in a relatively humid atmosphere. Depending on the aerosol species and the humidity of the environment, particles can take up water, changing their diameter and their optical properties. Does this affect VDR values or any metric by which the aerosol species were partitioned? Would it change the analysis in later sections at all, especially pertaining to attribution of fresh versus aged plumes?

VDR values of large non-spherical particles will be affected by humidity, in the sense that water absorption will make these particles more spherical, and hence decrease the associated VDR values. On the other hand, small pollution particles (local anthropogenic or resulting from biomass burning far south) generally do not depolarize much, at least not at the wavelength of the lidar. Therefore, the VDR value of pollution particles having taken up water will not be significantly modified (i.e. will remain within the uncertainty of the VDR retrieval method).

From the in-situ perspective, relative humidity might indeed affect some of the measurement properties (as correctly pointed out by the reviewer, the optical properties of more hygroscopic components of aerosols, for example). However, most of the aerosol sampling lines are heated (to 35-40°C), effectively limiting water uptake and relative humidity to values below 40%. Therefore aerosol properties derived from in-situ measurements are given for dry conditions.

Furthermore, the goal here is to obtain a general classification into aerosol types, achieved via a combination of collocated metrics, most of which (e.g. gas-phase, or total aerosol number > 10 nm) are typically insensitive to relative humidity. Therefore, the effect of aerosol water uptake is not considered to be a source of bias in the analysis presented here.

A sentence was added on this. See answer to next point.

Page 8 – Lines 181-182) What about urban O3? Will that mislead the speciation between smoke and pollution?

The O_3 measurements in the ATR are based on dual cell technology (a Thermo Environmental Instrument – TEI 49), and therefore largely insensitive to ambient relative humidity according to Spicer et al. (2010).

Spicer, C. W., D. W. Joseph and W. M. Ollison, 2010: A Re-Examination of Ambient Air zone Monitor Interferences, J. Air & Waste Manage. Assoc. **60**:1353–1364.

A couple of sentences were added after the description of the aerosol types (Section 2.1.2) in the revised manuscript to cover this point and the previous one:
"Gas phase and aerosol metrics above are typically insensitive to relative humidity. The aerosol sampling lines are heated (to 35-40°C), effectively limiting water uptake and relative humidity to values below 40%. The O_3 measurements in the ATR are based on dual cell technology, and therefore largely insensitive to ambient relative humidity according to Spicer et al. (2010), in spite of the humid environmental conditions over the Gulf of Guinea."

Page 8 – Line 202) It is stated that "data were processed with a time resolution of 1 s" – is this for all data or just the CAPS-Mex data? Was there some standard time resolution used for interpolation across instrumentations to line up the time resolutions? If so, what interpolation technique was used?

1 s resolution is for the CAPS-Mex data in that case. We have used the native resolution of the instrument or have averaged measurements to a coarser resolution, as indicated in Table 1 (note that we have completed Table 1 where this information was lacking). We have not attempted to line up the time evolution of the different instruments and therefore have not used any interpolation technique to plot the data.

Page 13 – Lines 322-324) Is this one-way or two-way nesting in WRF?

WRF is used to compute the meteorology and CHIMERE for the transport of chemical species and tracers. The CHIMERE model is forced off-line by WRF. The WRF simulations are performed before CHIMERE and independently of the species to transport. For WRF, it is two-ways nesting and for CHIMERE it is one-way nesting.

This information has been added in the revised manuscript (see reply to the subsequent comment).

Page 13 – Lines 326-327) More description of the WRF setup and physics options is necessary, especially the PBL parameterization, since the WRF PBL height is used later on in the paper. Furthermore, the WRF parameterizations used generally get a reference citation. Does the statement that the model configuration is the same as in Deroubaix et al. 2018 mean that every physics option / parameterization is identical to their setup? What about time steps, output intervals, and nudging? The Deroubaix et al., 2018 simulation was for a similar region in SWA, but the grid spacing was coarser, the simulation was run for a much longer duration to study short-term climate phenomena, and they ran with active chemistry instead of tracers. Stating that the setup is the same as in Deroubaix et al. 2018 may be confusing when these differences are considered.

The WRF set-up is strictly the same as the one fully described in Deroubaix et al. (2018), except of the grid spacing. The description of the schemes used in WRF was not included again in the present paper because the differences in resolution and duration have no impact on the choice of physics parameterizations. The fact that CHIMERE is running active chemistry or passive tracers is also independent of the choices made to calculate the meteorology with WRF. CHIMERE being used in off-line mode, the meteorology is calculated first, before the start of the CHIMERE simulation.

Nevertheless, for the sake of clarity and self-coherence, the text was changed and now reads:
"The WRF model (version v3.7.1, Shamarock and Klemp, 2008) and the CHIMERE chemistry-transport model (2017 version, Mailler et al., 2017) are used in this study. WRF calculates meteorological fields that are then used in off-line mode by CHIMERE to (i) conduct tracer experiments and (ii) compute backplumes. WRF and CHIMERE simulations are performed on common horizontal domains and with the same horizontal resolution. For the period 30 June–3 July 2016, two simulations are conducted for both WRF and CHIMERE to provide insights into the airborne observations: a simulation with a 10-km mesh size in a domain extending from 1°S to 14°N and from 11°W to 11°E (larger than the domain shown in Figure 1a) and a simulation with a 2-km mesh size in a domain extending from 2.8°N to 9.3°N and from 2.8°W to 3.3°E (Figure 1a).

The nested WRF simulations are first performed with hourly outputs. For the two horizontal resolutions, the same physical parameterizations are used and are those described in Deroubaix et al. (2018). The ABL scheme is the one proposed by the Yonsei University (Hong et al., 2006), the microphysics is calculated using the Single Moment-6 class scheme (Hong and Lim, 2006), the radiation scheme is RRTMG (Mlawer et al., 1997), the cumulus parameterization is the Grell-Dévényi scheme and the surface fluxes are calculated using the Noah scheme (Ek et al., 2003). The 10-km WRF simulation uses National Centers for Environmental Prediction (NCEP) Final global analyses as initial and boundary conditions. NCEP Real-Time Global SSTs (Thiébaux et al., 2003) are used as lower boundary conditions over the ocean. The meteorological initial and boundary conditions for the 2-km WRF simulation are provided by the 10-km WRF run, which, in turn, receives information from the 2-km WRF simulation (two-way nesting). The simulations are carried out using 32 vertical sigma-pressure levels from the surface to 50 hPa, with 6 to 8 levels in the ABL.

Then the CHIMERE simulations are performed. The horizontal grid is the same as for the lower resolution WRF runs. Vertically, CHIMERE uses 20 levels from the surface to 300 hPa and three-dimensional meteorological fields are vertically interpolated from the WRF to the CHIMERE grid. The two-dimensional fields, such as 10-m wind speed, 2-m temperature, surface fluxes and boundary-layer height are used directly in CHIMERE. The chemistry and aerosol initial and boundary conditions for the 2-km CHIMERE simulation are provided by the 10-km simulation (one-way nesting)."

Ek, M. B., Mitchell, K. E., Lin, Y., Rogers, E., Grunmann, P., Koren, V., Gayno, G., and Tarpley, J. D., 2003: Implementation of Noah land surface model advances in the National Centers for Environmental Prediction operational mesoscale Eta model, J. Geophys. Res.-Atmos., 108, 8851.

Hong, S. and Lim, J., 2006: The WRF single-moment 6-class microphysics scheme (WSM6), 42, 129–151.

Hong, S.-Y., Noh, Y., and Dudhia, J., 2006: A new vertical diffusion package with an explicit treatment of entrainment processes, Mon. Weather Rev., 134, 2318–2341.

Mlawer, E. J., Taubman, S. J., Brown, P. D., Iacono, M. J., and Clough, S. A., 1997: Radiative transfer for inhomogeneous atmospheres: RRTM, a validated correlated-k model for the longwave, J. Geophys. Res., 102, 16 663.

Page 14 – Lines 344-346) Is there any observational evidence or prior literature that supports scaling urban emissions by population in this way? For example, why couldn't an efficient metropolis have 5x the population as a baseline city, but only 2x the pollution? Does the linear scaling of population and pollution break down at some point for this region or other regions?

We agree with the reviewer: efficient megacities may have 5x the population compared to a 'baseline city' but only 2x the pollution. However, large cities of developing countries in West Africa are known not to be 'efficient' due to a lack of adequate policies. Here, our goal is to use tracers in CHIMERE to look at the spatio-temporal structure of city plumes, away from emissions and after transport. Considering that African cities generate an atmospheric pollution roughly proportional to their total population is as good a first guess as any. Furthermore, the differences in emissions scaled to the population for the cities of Accra and Lomé are not so different from Cotonou (3x and 1.8x, respectively), unlike Lagos (13x). However, Lagos emissions did not impact the air quality over the area of interest for this case study, as explained in the manuscript. Hence, even in the event that emissions are not strictly proportional to city population and that the 3x and 1.8x factors were slightly different, the conclusion drawn from the tracer experiments would not be changed.

Our approach would have been different if we wanted to relate a maximum of concentration observed with the aircraft over a city. In such a case, we would need to consider emissions density and then population density, not total population.

A sentence was added in the revised version of the manuscript:
"Large cities in developing countries are generally considered to generate an atmospheric pollution roughly proportional to their total population due to a lack of adequate emission policies."

Page 14 – Lines 347-349) The naming of the simulations is a bit counterintuitive. Instinctively, I'd think that TRA_D1 would represent July 1st and TRA_D2 as July 2nd. However, TRA_D2 is July 1st and TRA_D3 is July 2nd. By the time these simulations were discussed 13 pages later, the numbering became confusing. Perhaps numbering related to the dates would help readers later on (e.g. TRA_D12 = July 1st-2nd, TRA_D1= July 1st only, TRA_D2 = July 2nd only).

Agreed. We have modified the denomination of the experiments as suggested. Furthermore, experiment TRA_I1 was renamed TRA_I12 to be coherent with the naming of experiments TRA_Dx.

Page 14 – Lines 353-355) What does it mean that the lifetime of the tracers is designed to be 48 hours? Why set the concentration to zero if they are still present in the domain after 48 hours? Is it because the tracers do not undergo gravitational settling? Would including the gravitational settling process change the interpretation in later sections?

Sorry about the confusion here. The mention to a 48 h lifetime and setting concentrations to zero after that time is erroneous. This set up corresponds to previous model configurations, not the one used in this study and described in Mailler et al. (2017). The tracers are continuously emitted and there is no lifetime. The sentence, lines 353-355, was completely removed. About the settling, this process is not taken into account for the tracers as they are considered as 'gaseous' tracers.

Page 15 – Line 365) Why are the tracers released at 2500 m ASL?

This is based on the altitude of the elevated biomass burning layer arriving from the south (feature E seen in the Figure 3a). Since this information is provided later, we have added a sentence here to justify this.

The following sentences have been added in the revised manuscript (2nd and 4th sentences of Section 3.2.2):

"The objective is to assess the origin of an elevated aerosol layer observed with the lidar ULICE (see Section 5)."
"For both locations, backplumes are launched at 2500 m above sea level on 2 July 2016 at 17:00 UTC (i.e. the height of the elevated aerosol layer above the Gulf of Guinea, see Section 5)."

Page 18 – Lines 462-465) Maybe the placement of the 'A' on Figure 3 is misleading. To me, it looks like the 'A' is pointing to shallow clouds and not an aerosol layer.

We have added an arrow in Figure 3, to point to 'A' to make things clearer.

Mention to the added arrow is now made in the caption of Figure 3.

Page 20 – Line 503) Is there an explanation for why there is a reduction in O3 concentrations compared to background levels for Plume A?

Plume A is related to fresh anthropogenic emissions from Lomé, including NO_x. The addition of a large quantity of NO_x into the atmosphere can lead to a significant shift in the ozone chemical equilibrium, which can effectively result in near-source consumption, as observed here.

The following has been added in the revised version of the manuscript:
"[…] together with an O_3 concentration reduction (**Figure 5b**). Plume A is related to fresh anthropogenic emissions from Lomé, including NO_x. The addition of a large quantity of NO_x into the atmosphere can lead to a significant shift in the ozone chemical equilibrium, which can effectively result in near-source consumption, as observed here."

Page 20 – Line 506) What is the significance of the O3 to CO ratio? Why does the value of 0.15 imply the plume is fresh versus a value of 0.25 implies that it is aged?

The O_3/CO ratio is an indicator of the aging of air mass during transport. Whereas the actual O_3/CO ratio depends on a number of parameters, such as background CO, source emission profile, insolation, availability of O_3 precursors, atmospheric reactivity, etc…, to the first order the ratio increases as the plume is aging (e.g. Jaffe and Wigder, 2012, and Kim et al., 2013). This is because, in the troposphere, the ozone production continues as long as NO_x is available, whereas CO concentrations decrease slightly during transport. Hence, the actual increase of this ratio by 65% observed here is more meaningful than the values itself. To reflect this more clearly, the sentence on P.20 L.506 has been removed and P.20 L.517 has been modified to now read:

"The O_3/CO ratio (an indicator of air mass aging, e.g. Jaffe and Wigder (2012) and Kim et al. (2013)) observed to be associated with feature B increases with respect to feature A (0.25 vs. 0.15, i.e. a 65% increase), which is compatible with a further processed urban plume, as also corroborated by wind measurements. "

Jaffe, D. A. and N. L. Wigder, 2012: Ozone production from wildfires: A critical review, Atmos. Env., 51, 1-10.

Kim, P. S., D. J. Jacob, X. Liu, J. X. Warner, K. Yang, K. Chance, V. Thouret and P. Nedelec, 2013: Global ozone–CO correlations from OMI and AIRS: constraints on tropospheric ozone sources, Atmos. Chem. Phys., 13, 9321–9335.

Page 23 – Lines 592-593) This is regarding the statement that the emissions come only from July 1st. Figure 4 shows the wind speeds above 500 m to be weak (1-2 m/s), so the emissions on July 2nd haven't had a chance to be advected far from their source regions in the weak winds. It makes sense then that the emissions must be from July 1st, or an earlier date. Is it possible that due to the low wind speeds above the PBL that what we are seeing isn't just from July 1st, but also June 30th? Would the picture change if the tracers were released starting on June 30th?

If we compare Figure 7a (TRA_D12, new nomenclature proposed by the referee, previously TRA_D1) and 7d (TRA_D2, new nomenclature, previously TRA_D3), it is clear that the difference is related to emissions on 1 July and that the differences are observed above the marine ABL, in the region of the easterly flow (centered at ~1.5 km amsl) where the winds are not so weak. It is fair to say that emission from the 30 June will contribute to the overall picture, however, given the proximity of the western boundary of the 2-km CHIMERE domain to the western part of the aircraft flight track, we are confident that the tracers from 30 June would have been advected out of the domain in the afternoon of 2 July.

Page 26 – Lines 671-675) Do you think the maximum extent that the plume reaches over the ocean in the model is related to the tracer lifetime and the end time of the simulation? If the simulation was run for longer, would the maximum tracer extent over ocean increase? This goes back to the previous comment about releasing tracers on June 30th. If the tracers have no settling velocity or cannot be scavenged by precipitation, they could be advected indefinitely in the model.

There is no fixed lifetime for the tracers as explained above. We do acknowledge that this was not clear in the original version of the manuscript and it is only fair that the reviewer inquiries about this given the elements provided at the time.

The extent of the plume is mainly controlled by the direction of the mid-level easterly winds (and the small northerly component associated with it), as explained in Section 6.2.

We have re-emphasized this in the Conclusion by modifying the last sentence of the antepenultimate paragraph:
"[…]and (d) the tracer plumes do not extend very far over the ocean during the short period under scrutiny, mostly because they are transported northward within the marine ABL and westward above it so that their extent is controlled by the equatorward component in the mostly easterly flow as modulated by the synoptic-scale disturbances (Knippertz et al., 2017)."

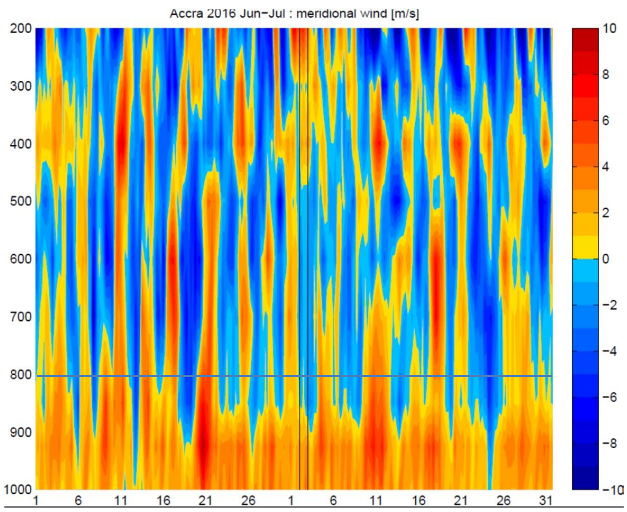

Furthermore, when looking at the meridional wind extracted over Accra over the months of June and July 2016 (see Figure to the left), we observe that at the mean altitude of the easterly flow above the monsoon flow (~800 hPa) there is an alternation of northerly and southerly components imposed by the propagation of African Easterly Waves. This alternation is really what limits the extent of the pollution plume over the ocean, as the meridional component changes from northerly to southerly every ~3 days during the 2 months.

Page 30 – Lines 751-752) Why is the correlation here related to terrain? I'm not sure I see the connection between skin temperature, vertical velocity, and terrain.

The meridional gradient of skin temperature between the sea and the land is an indicator for the pressure difference and thus drives the intensity of the southerly flow associated with the land sea breeze. When the southerly flow impinges on the low terrain over SWA, as it progresses over the continent, enhanced vertical motion is generated.

This information has been added in the revised version of the manuscript.

Page 35 – Lines 897-905) Was the flight over the Mediterranean an aerosol-free environment for calibration? If not, how might that affect the accuracy or uncertainty in the retrievals?

The ATR flight over the Mediterranean was conducted from an altitude above 6 km amsl, with ULICE lidar data acquired between 0 and 6 km amsl (see Figure below). The calibration was performed using lidar data acquired around 1528 UTC well above the aerosol layer, i.e. between 5 and 6 km amsl where the lidar backscatter is only sensitive to the molecular background signal.

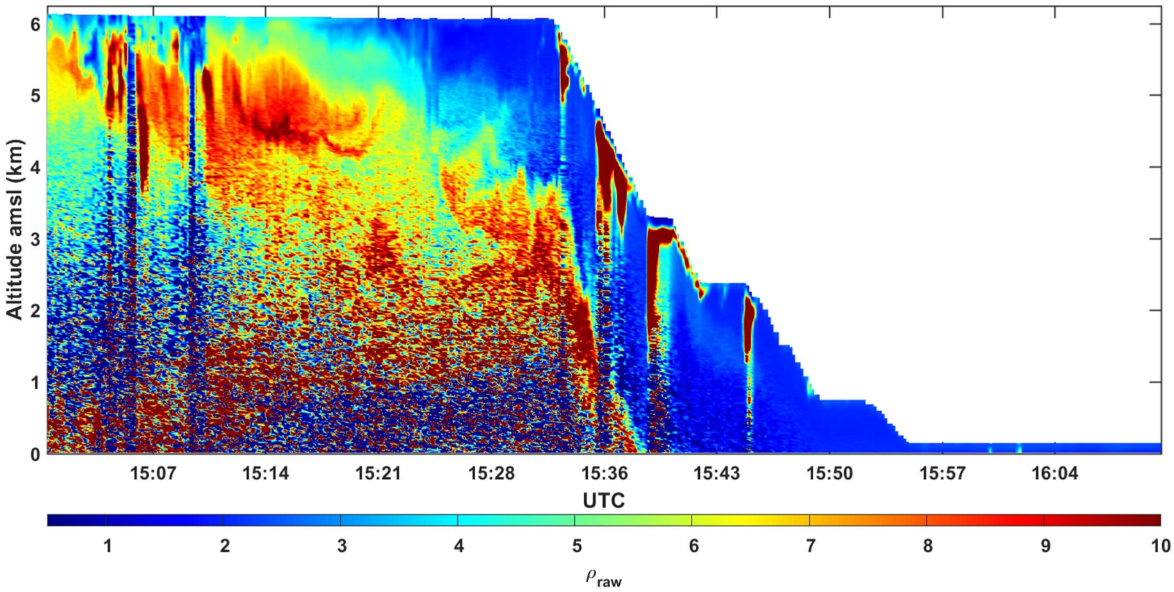

This information was added in the appendix of the revised manuscript, after the last paragraph:
"During the flight over the Mediterranean, the ATR was flying at an altitude of 6.3 km amsl, with ULICE lidar data acquired in the nadir pointing mode between 0 and 6 km amsl. The calibration was performed using lidar data acquired well above any aerosol layers, i.e. between 5 and 6 km amsl where the lidar backscatter is only sensitive to the molecular background signal."

Page 47 – Table 1) Not every entry has a time resolution associated with it. Also, if uncertainty estimates are available they should be listed here.

Agreed. We have included all information relevant to instrument resolution and uncertainty.

Page 65 – Figures a,b) From CALIOP we have aerosol speciation, as well as horizontal and vertical location, and from MODIS we have some idea of the concentration. What new information did the aircraft observations and tracer experiments provide the community that we did not already have with the MODIS AOD and CALIOP data?

MODIS and CALIOP data are invaluable in the regional and global context. Nevertheless, SWA, and particularly the coastal region, is prone to the presence of mid-level- and high-level water and ice clouds, which generally impair the lidar retrievals in the lower troposphere. This is evident for instance from Figure 10b where the classification is somewhat rudimental compared to the complex aerosol situation characterized with the combination of lidar and in situ data at high spatio-temporal resolution. With tracer simulations, we are able to distinguish between the plumes from the different cities. Furthermore, CALIOP aerosol classification retrievals are known to be error-prone in regions characterized by complex atmospheric dynamics such as SWA.

Page 2 Sup. Mat. – Lines 31-32) What is meant by variability across WRF grid boxes? Is this a standard deviation?

Yes, this is the standard deviation of observations contained within each grid box. We have modified this (changing 'variability' to 'standard deviation').

The last sentence of the caption was modified to:
"The mean value and standard deviation of the observations within WRF grid cells are indicated as dots and whiskers, respectively."

Page 2 Sup. Mat.) Was there moisture information available from the radiosondes or flight instruments? If so, how well did WRF do compared to the observations in terms of moisture? This also goes back to the point raised for Pg. 7-8 on how humid the environment was for this case study and how that might affect the retrievals.

Yes, such information was available from the radiosondes and the aircraft, but not shown in the paper. The figure on the right-side shows a comparison of the relative humidity derived from the radiosonde launched at 1700 UTC from Accra. Below 3 km amsl, the WRF simulation with a 2 km grid box and the observations match very well, and indicate that the condition were quite moist, relative humidity being essentially in excess of 80%, with a peak of 90% near the top of the marine ABL. Above 3 km amsl, the bias between observations and the simulation is larger, on the order of 10–15%.

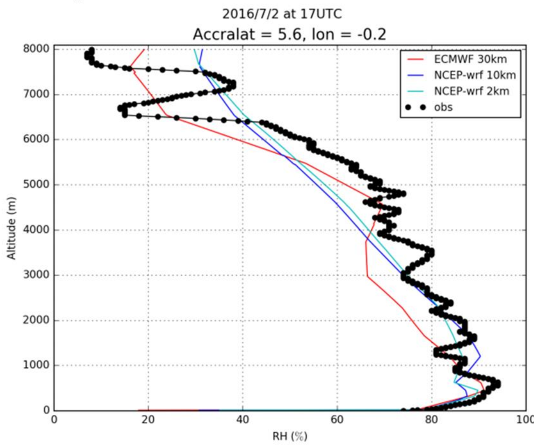

Page 3 Sup. Mat.) Is this following the trajectory of the balloon and matching it to the WRF grid boxes, or assuming it is constant in horizontal model space at the release site lat/lon at the surface?

For each sounding data the corresponding WRF grid cell value is extracted from the model data. In fact, a bilinear interpolation is performed horizontally to exactly match the horizontal position of the balloon. Linear interpolations are also performed vertically between two WRF levels as well as temporally between two consecutive model outputs to match the altitude of the balloon at the time the PTU observations are made.

This information is now added in the revised version of the manuscript, before Section 3.2.1, as it applies to both aircraft and balloon data:
"For each aircraft and sounding data point, the corresponding WRF grid cell value is extracted. A bilinear interpolation is performed horizontally to exactly match the horizontal position of the balloon or aircraft. Linear interpolations are also performed vertically between two WRF levels as well as temporally between two consecutive model outputs to match the altitude of the balloon or aircraft at the time the pressure, temperature, humidity and wind observations are made."

Technical Comments

Page 18 – Line 452) The word 'Possibly' should be lowercase
Corrected.

Page 18 – Line 457) Should this be Figure 5c and 5e instead of 4c and 4e?
Absolutely. Corrected.

Page 21 – Line 524) Missing word ‘of’ between ‘mixture long-lived’
Corrected.

Page 23 – Line 581) Magenta line
Corrected.

Page 32 – Line 803) The WRF / CHIMERE models
Corrected.

Page 35 – Line 886) Subscript ‘a’ on beta instead of ‘p’
Corrected.

Page 61 – Line 1205) Magenta line
Corrected.

Page 69 – Figure 12-c) Green and blue reference lines for land / ocean missing

We have looked into this. The figure with the green and blue reference lines have been added below for information (right-hand side) and comparison with the figure in the manuscript (left-hand side). We did not include the green and blue lines in the first place because we feel they are misleading for the reader. They give the impression that the aircraft takes off far inland and that half of the flight is over land. This is because, as stated in the manuscript, "[…] Surface characteristics are defined based on the dominating surface type in the latitudinal band considered for the average of the wind field […]". Therefore, we have decided not to include the blue and green lines in Figure 12c.

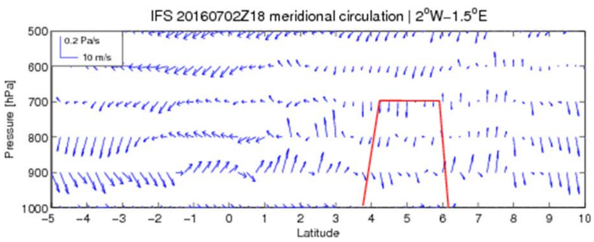

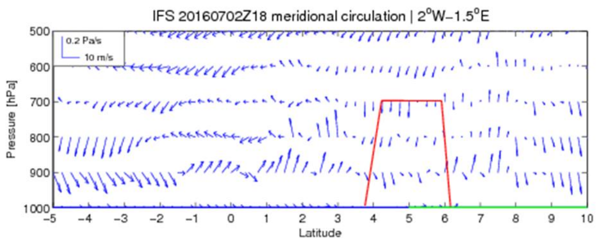

Page 3 Sup. Mat. – Line 38) Missing UTC from 1700 and 1612
Corrected

Page 4 Sup. Mat.) Missing a reference arrow for wind speeds
An arrow has been added in the revised figures S3a, b as shown below.

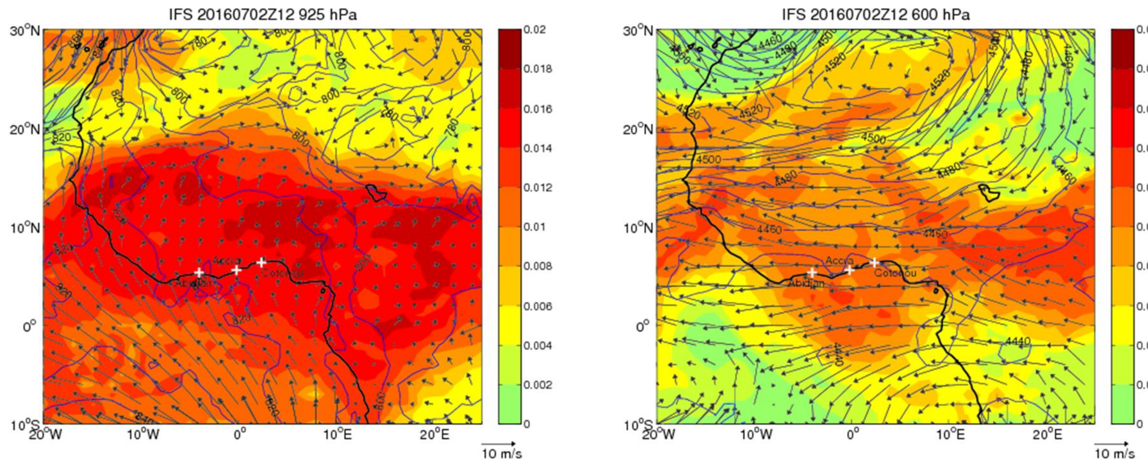

Referee #2 comments

This paper presents a day in the life of the airborne Dynamics-Aerosol-Chemistry-Cloud Interactions in West Africa project. Conclusions are drawn regarding the role of both synoptic and mesoscale meteorological features as well as the contributions nature of different sources on the aerosol environment. Overall, it is a reasonable analysis, but given it is really a one day analysis, it is difficult to support their findings in general. I myself use "a day in the life" sorts of papers to describe various phenomenon in a region in detail. But, such papers are always in a context of subsequent papers that then generalize. Here, the single day is used to generalize, which almost by definition leads to unsupportable overall conclusions. e.g., can you really say a city's emissions are unimportant at some point based on a single day's analysis? This particular flight was pretty much parallel to the coast, such that the real littoral transition was never observed. I strongly recommend that the paper be reworked such that this one demonstrates key features. Showing a day in the life of the role if individual cities or meteorological phenomenon is worthy of publication if framed that way. But, generalization will need to happen with the support of a much more comprehensive airborne, satellite and modeling study of the entire field campaign to determine. As is I am not sure what to make of the paper or how it will be used by the community. Most of the work here is wordsmithing, so I do not think it is an overly onerous task to reframe in this way.

We would like to thank the reviewer for his/her comments on the paper. We now also acknowledge the work of the anonymous referee in the acknowledgement section of the paper.

I pretty much agree with the other reviewer on specifics, where again a lot of generalization is made on a single observation.

The flight made in the afternoon of 2 July is unique in the sense that it is the only flight conducted over the ocean during which the downward looking lidar ULICE was operational. The combination of remote sensing to monitor the aerosol landscape over the Gulf of Guinea and in situ measurements to assess the nature of the observed aerosols was only possible on that day. For information, two other so-called OLACTA flights were conducted with the ATR 42 during the campaign. However, the lidar was not working and only in situ, low-level measurements were made.

Regarding the generalization aspect of the comment, we would like to emphasize that regarding the zonal circulation we have conducted a short but significant analysis of its occurrence in the course of July 2016. As stated in the manuscript, the zonal circulation is a general feature of July 2016 and not only unique to the 02 July 2016. Other statements such as the lack of impact of Lagos emissions on the region to the west of Cotonou were not meant to be general, but indeed specific to the case under scrutiny. This was not our objective to generalize results for the case study. Therefore, we have edited the content of the Abstract and Conclusion in order make it clearer that the results are case dependent, not general to the post-onset period at the coast of SWA.

Here are a few more minor comments to consider.

On using AAE to speciate-line118: I am a bit concerned about using the AAE to say what the makeup of particles are given that by the analysis here there is often a mixture of aerosol species. This is further complicated for dust, which from aircraft inlets have a low penetration efficiency.

We agree that homogeneous plumes for a given aerosol type will likely only be observed fairly close to the sources, and that in the broader area of the aircraft operation, mixing is likely to occur. Rather than indicating homogeneous plumes, our metrics are an indication of what type of aerosol dominates the composition of a given sampled air mass. This is now more clearly stated in the revised manuscript (see reply to Referee#1 above on the same topic).

We would like to emphasize that AAE is to the first order sensitive to the composition of the sampled aerosols. AAE values are rather insensitive to the size distribution of sampled aerosols. Therefore, even though aerosol measurements may be affected by the inlet efficiency, the derived AAE will still be a good indicator for discriminating plumes dominated by dust, biomass burning and urban aerosols.

This information is now added in the revised version of the manuscript, in Section 2.1.2 shortly after AAE is introduced:
"AAE values are rather insensitive to the size distribution of sampled aerosols. Therefore, even though aerosol measurements may affected by the inlet efficiency, the derived AAE will still be a good indicator for discriminating plumes dominated by dust, biomass burning and urban aerosols (e.g. Kirchstetter et al., 2004; Bergstrom et al., 2007; Toledano et al., 2007; Russell et al., 2010)."

Russell, P. B., Bergstrom, R. W., Shinozuka, Y., Clarke, A. D., DeCarlo, P. F., Jimenez, J. L., Livingston, J. M., Redemann, J., Dubovik, O., and Strawa, A.: Absorption Angstrom Exponent in AERONET and related data as an indicator of aerosol composition, Atmos. Chem. Phys., 10, 1155-1169, https://doi.org/10.5194/acp-10-1155-2010, 2010.

Bergstrom R W, Pilewskie P, Russell P, Redemann J, Bond T, Quinn P, Sierau B. Spectral absorption properties of atmospheric aerosols. Atmospheric Chemistry and Physics 2007;7(23):5937-43.

Toledano, C. , Cachorro, V. E., Berjon, A. , de Frutos, A. M., Sorribas, M. , de la Morena, B. A. and Goloub, P. (2007), Aerosol optical depth and Ångström exponent

climatology at El Arenosillo AERONET site (Huelva, Spain). Q.J.R. Meteorol. Soc., 133: 795-807. doi:10.1002/qj.54

Kirchstetter, T. W., Novakov, T., Hobbs, P.V., 2004. Evidence that the spectral dependence of light absorption by aerosols is affected by organic carbon. J. Geophys. Res. 109, D21208.doi:10.1029/2004JD004999.

CAPS and Nephelometer-line 203: Again, the authors need to be mindful of dust particle penetration efficiencies and what that does to the interpretation of their results? I bring this up because based on the sounding of figure 4 this level is in an area of some wind shear.

Yes vertical wind shear could induce some mixing of the elevated dust towards the surface. However, the in situ measurements clearly show that the air masses below 2.5 km are dominated by other type of aerosols than dust.

Figure 3 and 6. Instead of using time as an x axis, can you please use distance or perhaps longitude (given the aircraft track) so we can get a spatial perspective.

We have added the information in the caption of the 2 figures, as distance (not longitude because of the aircraft turn after the end of the aircraft sounding).

A sentence was added at the end of the caption of Figure 3:
"The distance covered by the ATR 42 along this transect is ~450 km."

Likewise a sentence was added at the end of the caption of Figure 6:
"The distance covered by the ATR 42 along this transect is ~395 km."

We also have added information in the caption of Figure 2 regarding the coordinates of the lower left and upper right corners of the satellite images.

A sentence was added at the end of the caption of Figure 2:
"The coordinates of the lower left corner of the images are 0°N/8°W, and the coordinates of the upper right corner of the images are 13°N/10°45'E."

Figure 5-F. As well as number, can you please provide a profile of aerosol volume? It is much easier to interpret.

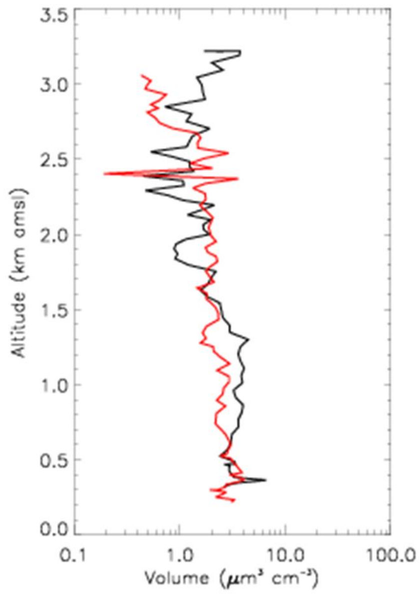

We have produced the vertical profiles of volume size distribution derived from the GRIMM OPC over the ocean (red solid line) and at the coast in the vicinity of Lomé (black solid line).

We do not feel like this plot adds much to the discussion of the results and decided not to include it.

Figure 9. What happens if you have a minor change in altitude of release? This will show you how sensitive your system is.

This has been tested. In the manuscript we only mention the fact that the structure of the backplume was unchanged when changing slightly the location starting point.

A similar sensitivity analysis was conducted by changing the altitude of the backplume end point and the result show that the sensitivity is low. Below, we compare the backplume for the same end point (Accra) but for 2 different altitudes: 2500 m amsl (left) and 3500 m amsl (right). The main message remains that plumes are coming with air masses originated in Central Africa and are transported to the north above the ocean.

This information is now added in the revised version of the manuscript at the end of Section 3.2.2 on "Backplumes":
"A similar sensitivity analysis is conducted by changing the altitude of the backplume from 2500 m to 3500 m amsl but the effect is small (not shown)."

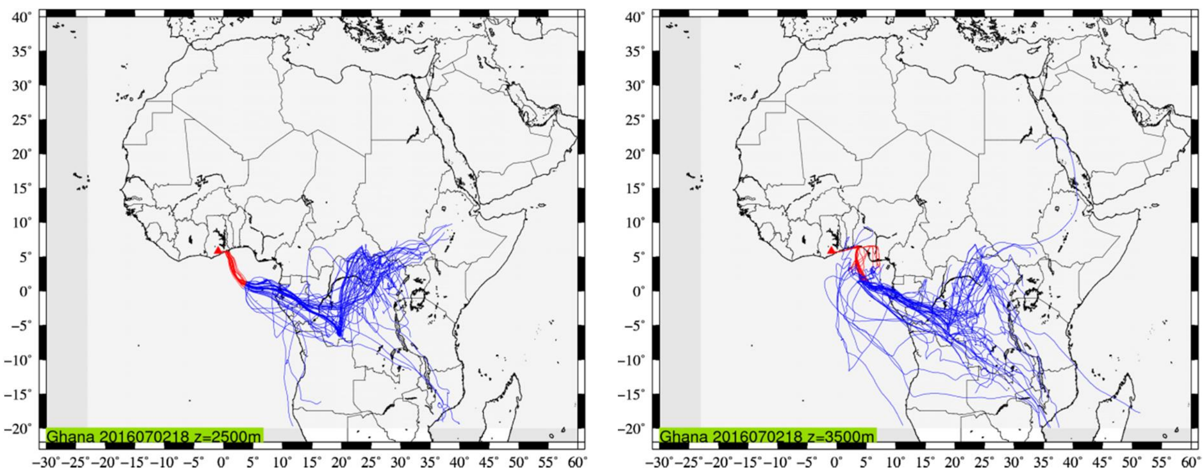

Supplemental Material

Aerosol distribution in the northern Gulf of Guinea: local anthropogenic sources, long-range transport and the role coastal shallow circulations

Cyrille Flamant[1], Adrien Deroubaix[1,2], Patrick Chazette[3], Joel Brito[4], Marco Gaetani[1], Peter Knippertz[5], Andreas H. Fink[5], Gaëlle de Coetlogon[1], Laurent Menut[2], Aurélie Colomb[4], Cyrielle Denjean[6], Remi Meynadier[1], Philip Rosenberg[7], Regis Dupuy[4], Pamela Dominutti[4], Jonathan Duplissy[8], Thierry Bourrianne[6], Alfons Schwarzenboeck[4], Michel Ramonet[3] and Julien Totems[3]

Mis en forme : Exposant

[1]Laboratoire Atmosphères Milieux Observations Spatiales, Sorbonne Université, Université Paris-Saclay and CNRS, Paris, France

[2]Laboratoire de Météorologie Dynamique, Ecole Polytechnique, IPSL Research University, Ecole Normale Supérieure, Université Paris-Saclay, Sorbonne Université, CNRS, Palaiseau, France

[3]Laboratoire des Sciences du Climat et de l'Environnement, CEA, CNRS, Université Paris-Saclay, Gif-sur-Yvette, France[4]Laboratoire de Météorologie Physique, Université Clermont Auvergne, CNRS, Clermont-Ferrand, France

[5]Institute of Meteorology and Climate Research, Karlsruhe Institute of Technology, Karlsruhe, Germany

[6]Centre National de Recherches Météorologiques, Météo-France and CNRS, Toulouse, France

[7]Institute of Climate and Atmospheric Science, School of Earth and Environment, University of Leeds, Leeds, United Kingdom

[8]Helsinki Institute of Physics, University of Helsinki, Helsinki, Finland

Comparison between WRF dynamics at 2-km, aircraft and radiosounding observations

(a)

(b)

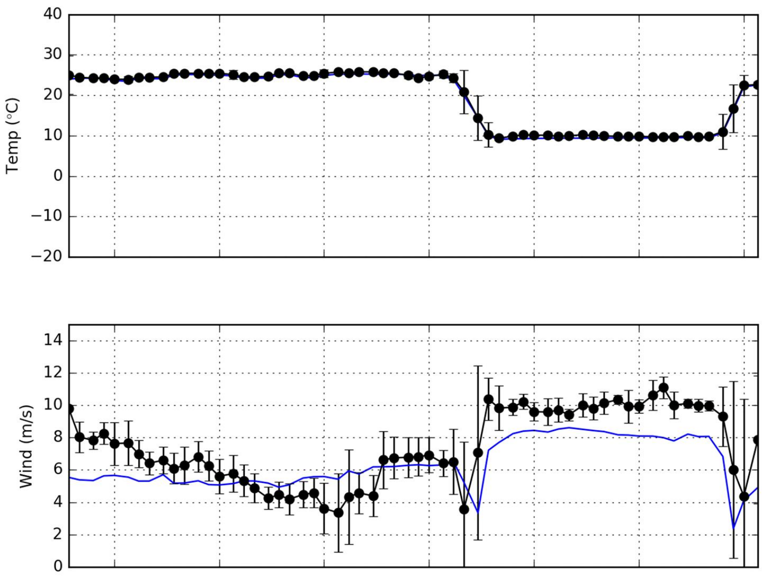

Figure S1: Evolution of temperature (a) and wind speed (b) along the ATR 42 flight track for in situ observations (closed black circles) and WRF (blue solid line). The ~~variability~~ mean value and standard deviation of the observations within WRF grid cells ~~is~~ are indicated as dots and whiskers, respectively.

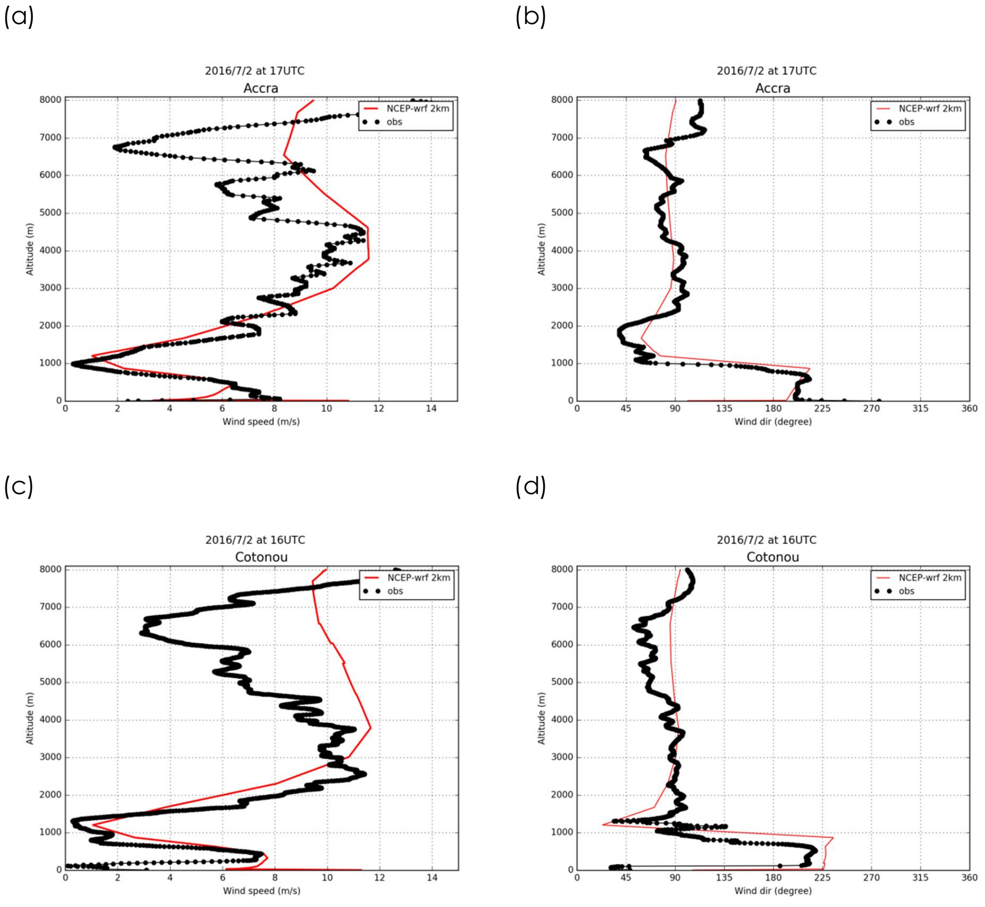

Figure S2: Wind speed (left column) and wind direction profiles (right column) in Accra (a and b, respectively) and Cotonou (c and d, respectively). Observations are shown as black dots and 2-km WRF simulations are shown as red solid lines. The radiosoundings were released at 1700 and 1612 UTC in Accra and Cotonou, respectively.

Regional scale dynamics from IFS

(a)

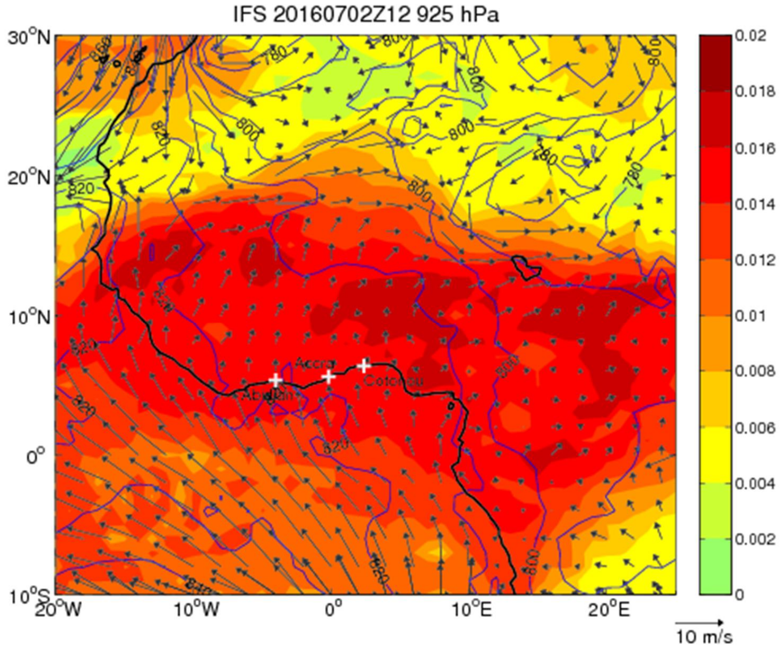

(b)

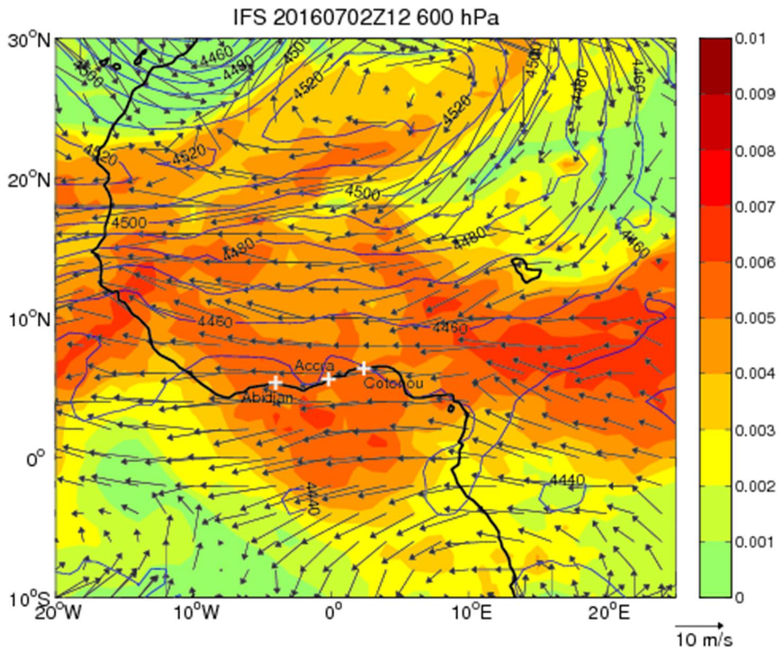

Figure S3: ECMWF IFS analyses at 1200 UTC on 2 July for water vapor mixing ratio (kg kg^{-1}, color shading), wind (vectors) and geopotential height (m, blue solid lines) at (a) 925 hPa and (b) 600 hPa. The African continent coastline is shown as a black solid line and cities of interest are indicated.

Regional scale aerosol composition from IFS-CAMS

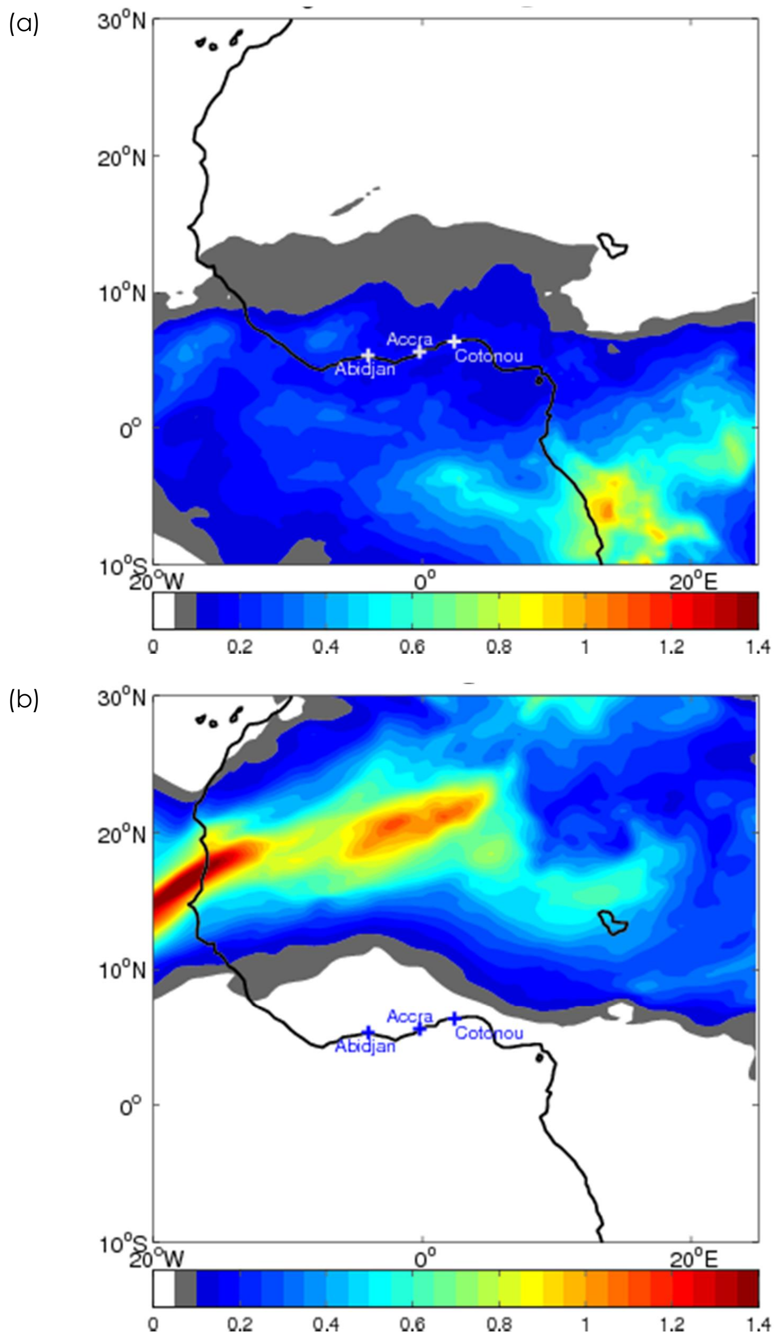

Figure S4: ECMWF CAMS forecast on 2 July 2016 at 1200 UTC (+12h forecast) for (a) organic matter AOD and (b) dust AOD. The African continent coastline is shown as a black solid line and cities of interest are indicated.

Regional overturning circulation induced by land-sea skin temperature gradients

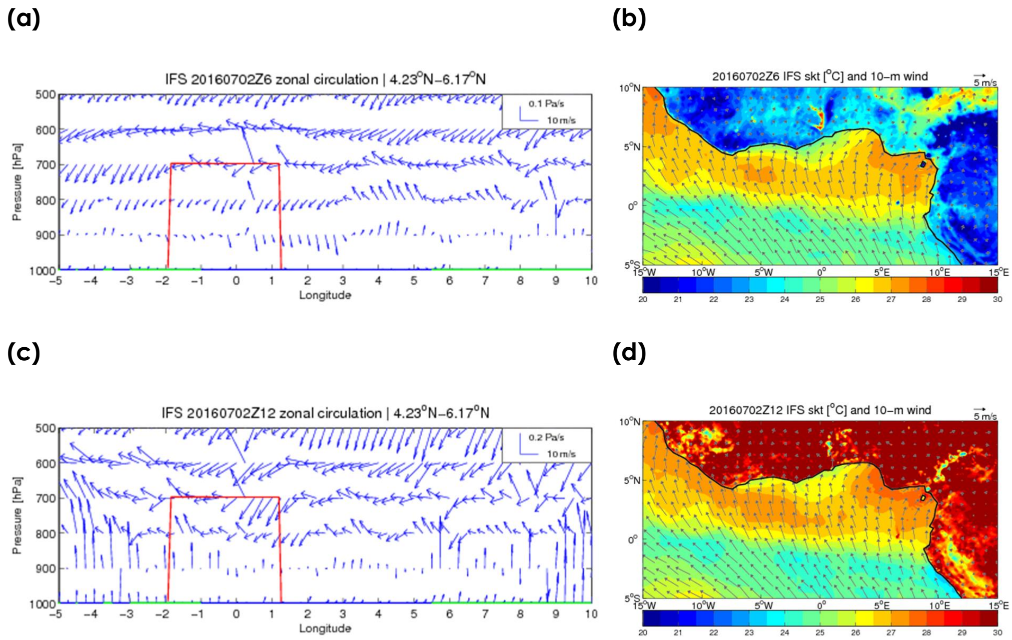

Figure S5: Left column: West–east oriented vertical cross section (1000–500 hPa) of zonal-vertical wind vectors from IFS analyses (blue) between 5°W and 10°E averaged between 4.54°N and 6.28°E at (a) 0600 and (c) 1200 UTC on 2 July 2016. The thick red line is the projection of the ATR 42 aircraft track onto the cross-section. The thick green and blue lines at the bottom of the graph indicate the presence of land and ocean, respectively. Surface characteristics are defined based on the dominating surface type in the latitudinal band considered for the average of the wind field. Right column: IFS skin temperature (colors) and wind field at 10 m (vectors) at (b) 0600 UTC and (d) 1200 UTC. Cross-sections (a) and (c) are computed in the zonal box shown in **Figure 12c** ~~in~~ of the main paper.

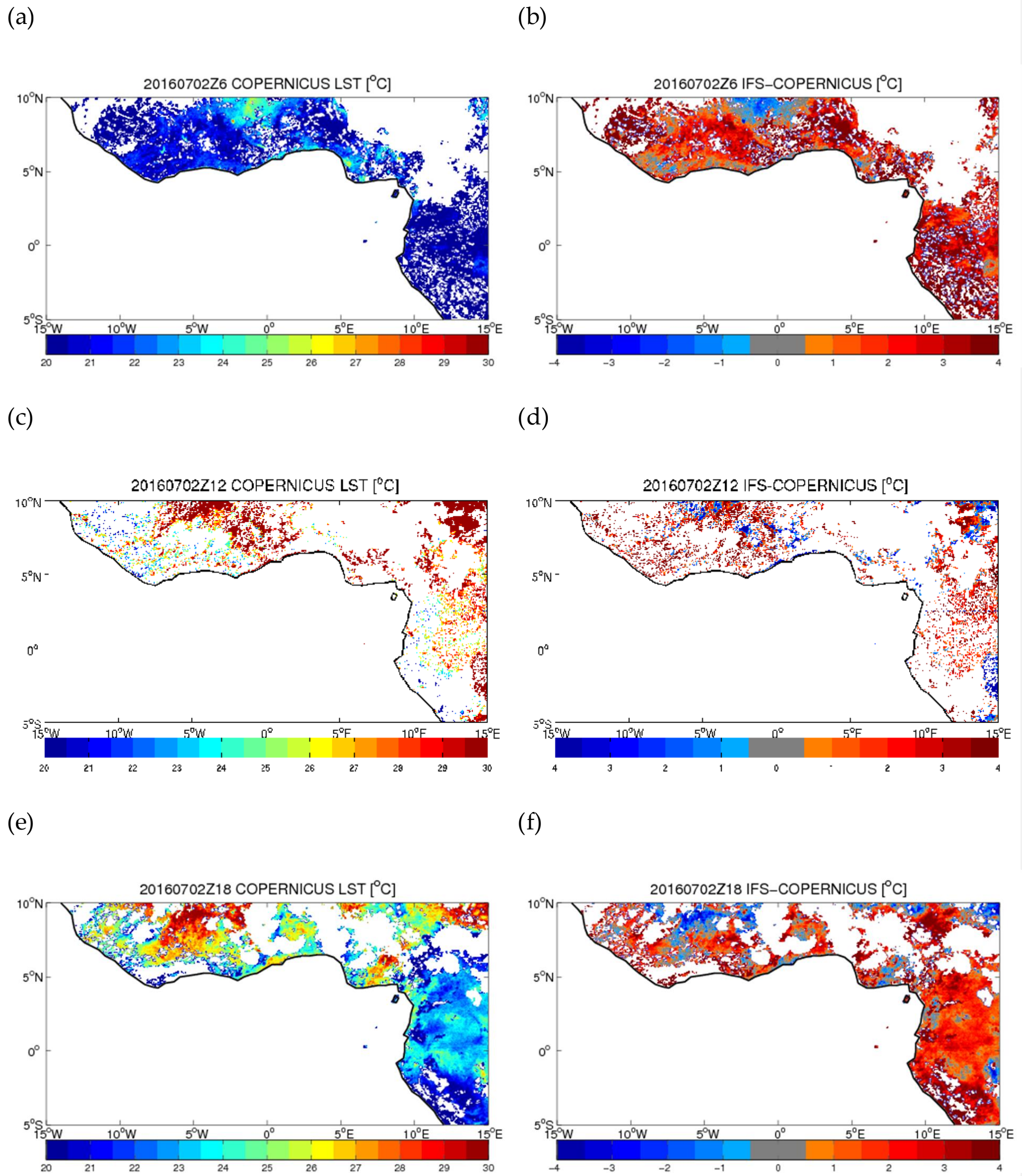

Figure S6: Left column: Copernicus skin temperature at (b) 0600 UTC, (d) 1200 UTC and (f) 1800 UTC on 2 July 2016. Right column: IFS minus Copernicus skin temperature at (b) 0600 UTC, (d) 1200 UTC and (f) 1800 UTC. IFS skin temperature, originally at 0.125° resolution, has been linearly interpolated onto the Copernicus grid at 5 km before computing the differences.

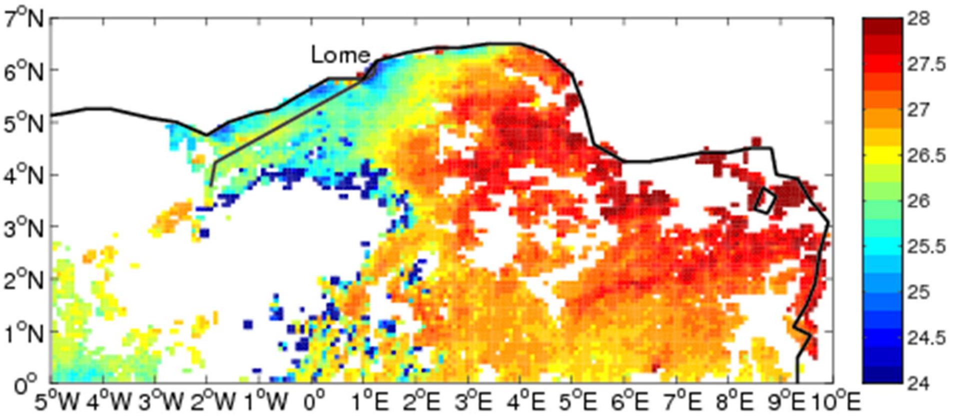

Figure S7: MODIS-derived SST on 2 July 2016, with superimposed ATR 42 flight track (black thick line).

Aerosol distribution in the northern Gulf of Guinea: local anthropogenic sources, long-range transport and the role of coastal shallow circulations

Cyrille Flamant[1], Adrien Deroubaix[1,2], Patrick Chazette[3], Joel Brito[4], Marco Gaetani[1], Peter Knippertz[5], Andreas H. Fink[5], Gaëlle de Coetlogon[1], Laurent Menut[2], Aurélie Colomb[4], Cyrielle Denjean[6], Remi Meynadier[1], Philip Rosenberg[7], Regis Dupuy[4], Pamela Dominutti[4], Jonathan Duplissy[8], Thierry Bourrianne[6], Alfons Schwarzenboeck[4], Michel Ramonet[3], and Julien Totems[3]

[1]Laboratoire Atmosphères Milieux Observations Spatiales, Sorbonne Université, Université Paris-Saclay and CNRS, Paris, France

[2]Laboratoire de Météorologie Dynamique, Ecole Polytechnique, IPSL Research University, Ecole Normale Supérieure, Université Paris-Saclay, Sorbonne Université, CNRS, Palaiseau, France

[3]Laboratoire des Sciences du Climat et de l'Environnement, CEA, CNRS, Université Paris-Saclay, Gif-sur-Yvette, France

[4]Laboratoire de Météorologie Physique, Université Clermont Auvergne, CNRS, Clermont-Ferrand, France

[5]Institute of Meteorology and Climate Research, Karlsruhe Institute of Technology, Karlsruhe, Germany

[6]Centre National de Recherches Météorologiques, Météo-France and CNRS, Toulouse, France

[7]Institute of Climate and Atmospheric Science, School of Earth and Environment, University of Leeds, Leeds, United Kingdom

Mis en forme : Exposant

Mis en forme : Non Exposant/ Indice

[8]Helsinki Institute of Physics, University of Helsinki, Helsinki, Finland

Mis en forme : Exposant

Abstract

The complex vertical distribution of aerosols over coastal southern West Africa (SWA) is investigated using airborne observations and numerical simulations. Observations were gathered on 2 July 2016 offshore of Ghana and Togo, during the field phase of the Dynamics-Aerosol-Chemistry-Cloud Interactions in West Africa project. The aerosol loading in the lower troposphere includes emissions from coastal cities (Accra, Lomé, Cotonou and Lagos) as well as biomass burning aerosol and dust associated with long-range transport from Central Africa and the Sahara, respectively. Our results indicate that the aerosol distribution on this day is impacted by subsidence associated with zonal and meridional regional-~~–~~scale overturning circulations associated with the land-sea surface temperature contrast and orography over Ghana and Togo. Numerical tracer release experiments highlight the dominance of aged emissions from Accra on the observed pollution plume loadings over the ocean, in the area of aircraft operation. The contribution of aged emission from Lomé and Cotonou is also evident above the marine boundary layer. Given the general direction of the monsoon flow, the tracer experiments indicate no contribution from Lagos emissions to ~~do not play a role~~impact the atmospheric composition ~~for~~of the area west of Cotonou, where our airborne observations ~~a~~were gathered. The tracer plume does not extend very far south over the ocean (i.e. less than 100 km from Accra), mostly because emissions are transported northeastward near the surface over land and westward above the marine atmospheric boundary layer. The latter is possible due to interactions between the monsoon flow, complex terrain and land-sea breeze systems, which support the vertical mixing of the urban

Mis en forme : Police :Italique

pollution. This work sheds light on the complex – and to date undocumented – mechanisms by which coastal shallow circulations distribute atmospheric pollutants over the densely populated SWA region.

1. Introduction

Aerosol-cloud-climate interactions play a fundamental role in radiative balance and energy redistribution in the tropics. Aerosol particles from natural and anthropogenic origins can serve as cloud condensation nuclei (Haywood and Boucher, 2000; Carslaw et al., 2010) and interact with solar and terrestrial radiation through absorption and scattering.

The atmosphere over southern West Africa (SWA) is a complex mix of local emissions (vegetation, traffic, domestic and waste fires, power plants, oil and gas rigs, ships) and remote sources (dust from the north and wild-fire related biomass burning aerosols from Central Africa) (Knippertz et al., 2015a, Brito et al., 2018). In order to enhance our understanding of aerosol-cloud-climate interactions in SWA, it is of paramount importance to better characterize the composition and vertical distribution of the aerosol load over the eastern tropical Atlantic. This is particularly vital, since SWA is currently experiencing major economic and population growths (Liousse et al., 2014), and is projected to host several megacities (cities with over 10 million inhabitants) by the middle of the 21st century (World Urbanization Prospect, 2015). This will likely boost anthropogenic emissions to unprecedented levels and imply profound impacts on population health (Lelieveld et al., 2015), on the radiative budget over SWA and also on the West African Monsoon (WAM) system (Knippertz et al., 2015b). This will also add to the dust and biomass burning aerosol related perturbations already evidenced for the precipitation in the area (e.g. Huang et al., 2009). Likewise, urban pollution may also affect surface-atmosphere interactions and associated lower tropospheric dynamics over SWA as for instance dust over the tropical Atlantic (e.g. Evan et al., 2009) or biomass burning aerosols over Amazonia (Zhang et al., 2008, 2009).

One of the aims of the EU-funded project Dynamics-Aerosol-Chemistry-Cloud Interactions in West Africa (DACCIWA, Knippertz et al., 2015b) is to understand the influence of atmospheric dynamics on the spatial distribution of both anthropogenic and natural aerosols over SWA after emission. One particularly important aspect is the fate of anthropogenic aerosols emitted at the coast as they are being transported away from the source. In addition, DACCIWA aims at assessing the impact of this complex atmospheric composition on the health of humans and ecosystems.

Urban aerosols are mostly transported with the southwesterly monsoon flow below 700 hPa (e.g. Deroubaix et al., 2018). They may also reach the nearby ocean as the result of complex dynamical interactions between the monsoon flow, the northeasterly flow from the Sahel above and the interactions with the atmospheric boundary layer (ABL) over the continent coupling the two layers when it is fully developed during daytime. This is because, as opposed to the marine ABL, the continental ABL exhibits a strong diurnal cycle (e.g. Parker et al., 2005; Lothon et al., 2008; Kalthoff et al., 2018). On hot, cloud-free summer days, land-sea breeze systems can develop at the coast (in conditions of moderate background monsoon flow, Parker et al., 2017), which contribute to the transport of pollutants emitted along the urbanized coastal strip of SWA.

The main objective of the present study is to understand how the lower tropospheric circulation over SWA shapes the urban pollution plumes emitted from coastal cities such as Accra, Lomé, Cotonou and Lagos, both over the Gulf of Guinea and inland. Here, we take advantage of the airborne measurements acquired during the DACCIWA field campaign (June–July 2016, Flamant et al., 2018) as part of the European Facility for Airborne Research (EUFAR) funded Observing the Low-level Atmospheric Circulation in the Tropical Atlantic (OLACTA) project to assess the characteristics of different aerosol layers observed over the Gulf of Guinea. To study the role of atmospheric dynamics on aerosol spatial distribution, we use a unique combination of airborne observations from the 2 July 2016, space-borne observations and finally high-resolution simulations performed using the Weather and Research Forecast (WRF) and CHIMERE models. The flight made in the afternoon of 2 July is unique in the sense that it is the only flight conducted over the ocean during which a downward looking lidar was operational. The combination of remote sensing to monitor the aerosol landscape over the Gulf of Guinea and in situ measurements to assess the nature of the observed aerosols was only possible on that day.

The airborne and space-borne data used in this paper are presented in Section 2, whereas the simulations are detailed in Section 3. Section 4 presents the synoptic situation and airborne operations over SWA on 2 July 2016. Atmospheric composition over the Gulf of Guinea as observed from aircraft in situ and remote sensing data is discussed in Section 5. Insights into the distribution of anthropogenic aerosols from tracer experiments are presented in Section 6 and long-range transport of aerosols related to regional-scale dynamics is described in Section 7. The influence of lower-tropospheric overturning circulations induced by the land-sea surface temperature gradient on the vertical distribution of aerosols over SWA is discussed in Section 8. In Section 9, we summarize and conclude.

2. Data

2.1 Airborne observations

During the DACCIWA field campaign, airborne operations on the afternoon of 2 July 2016 were conducted with the ATR 42 of the Service des Avions Français Instrumentés pour la Recherche en Environnement (SAFIRE) over the Gulf of Guinea (**Figure 1**). The afternoon flight was carried out in the framework of the EUFAR OLACTA project (Flamant et al., 2018). The aircraft was equipped with in situ dynamical and thermodynamical probes (yielding mean and turbulent variables), as well as in situ aerosol and cloud probes, and gas phase chemistry instruments. It also carried several radiometers (upward and downward looking pyranometers and pyrgeometers) as well as the Ultraviolet Lidar for Canopy Experiment (ULICE, Shang and Chazette, 2014). **Table 1** summarizes the instruments used in this study (see the Supplement of Flamant et al., 2018 for the complete ATR 42 payload during the field campaign).

2.1.1 ULICE observations

The ULICE system was specifically designed to monitor the aerosol distribution in the lower troposphere. During the DACCIWA field campaign, ULICE was pointing to the nadir. The system's nominal temporal and along-line-of-sight resolutions are 100 Hz and 15 m, respectively. In the present study, we use lidar-derived profiles of aerosol-related properties averaged over 1000 laser shots (~10 s sampling).

The ULICE receiver implements two channels for the detection of the elastic backscatter from the atmosphere in the parallel and perpendicular polarization planes relative to the linear polarization of the emitted light. The design and the calculations to retrieve the depolarization properties are explained in Chazette et al. (2012). Using co- and cross-polarization channels, the lidar allows identifying non-spherical particles in the atmosphere such as dust. The overlap factor is nearly identical for the two polarized channels, thereby permitting the assessment of the volume depolarization ratio (VDR) very close to the aircraft (~150 m).

Lidar-derived extinction coefficient profiles (as well as other optical properties) are generally retrieved from so-called inversion procedures as abundantly described in the literature (e.g. Chazette et al., 2012). During the DACCIWA field campaign the lack of adequate observations did not allow us to perform proper retrievals of aerosol optical properties using such procedures. Hence, in the following we only use the apparent scattering ratio (ASR, the ratio of the total apparent backscatter coefficient to the molecular apparent backscatter coefficient denoted R_{app}) and the VDR. Details are given in **Appendix A**, together with the characteristics of the lidar system.

Generally speaking, the VDR values observed during the flight are not very high and absolute values may be subject to biases. Nevertheless, relative fluctuations of VDR are accurately measured and useful as indicators of changes in aerosol properties.

2.1.2 Aerosol and gas phase chemistry measurements

For this study, we focus on available observations that can provide insights into the origin of the aerosol distribution over coastal SWA, namely biomass burning aerosols, dust and urban pollution. Because of the complex atmospheric dynamics in the area, we cannot assume that only homogeneous air masses will be sampled with the aircraft. Rather, the selected observations are indicators of which type of aerosol dominates the composition of a given sampled air mass:

- **Biomass burning aerosols**: identification was conducted at times of enhanced ozone (O_3) and carbon monoxide (CO) mixing ratios as well as aerosol parameters such as light absorption/extinction and number concentration.
- **Urban pollution**: the main tracers used were CO, nitrogen oxide (NOx) and total (>10 nm) particle number concentrations;
- **Terrigenous aerosols (dust)**: layers were identified at times of enhanced aerosol parameters (particularly super micron aerosols), in complement to the lidar-derived VDR observations and not followed by CO or O_3 enhancements (mostly associated with biomass burning here).

Sea salt cannot formally be identified with the in situ measurements conducted with the ATR 42 payload during DACCIWA. Gas phase and aerosol metrics above are typically insensitive to relative humidity. The aerosol sampling lines are heated (to 35-40°C), effectively limiting water uptake and relative humidity to values below 40%. The O_3 measurements in the ATR are based on dual cell technology, and therefore largely insensitive to ambient relative humidity according to Spicer et al. (2010), in spite of the humid environmental conditions over the Gulf of Guinea.

Mis en forme : Interligne : Double

In addition, absorption Angstrom exponent (AAE) measurements are used to distinguish urban air pollution from biomass burning smoke (Clarke et al., 2007) and mineral dust (Collaud Coen et al., 2004). In general the AAE values for carbonaceous particles are ~1 for urban pollution, between 1.5 and 2 for biomass smoke and around 3 for dust (Bergstrom et al., 2007). AAE values are rather insensitive to the size distribution of sampled aerosols. Therefore, even though aerosol measurements may be affected by the inlet efficiency, the derived AAE will still be a good indicator for discriminating plumes dominated by dust, biomass burning and urban aerosols (e.g. Kirchstetter et al., 2004; Bergstrom et al., 2007; Toledano et al., 2007; Russell et al., 2010).

The Particle Soot Absorption Photometer (PSAP, model PSAP3L) measures the aerosol optical absorption coefficient at three wavelengths (467, 530 and 660 nm) with a sampling time of 10 s. The data were corrected for multiple scattering and shadowing effects according to Bond et al. (1999) and Müller et al. (2009). Data with filter transmission under 0.7 are removed as corrections are not applicable. Furthermore, PSAP measurements were used to compute the AAE. The particle extinction coefficient is measured with a cavity attenuated phase shift particle light extinction monitor (CAPS-PMex, Aerodyne Research) operated at the wavelength of 530 nm. Data were processed with a time resolution of 1 s. An integrated nephelometer (Ecotech, model Aurora 3000) provided aerosol light scattering at three wavelenghts (450, 550 and 700 nm), which was used to correct for the impact of aerosol scattering based on the correction scheme by Anderson and Ogren (1998) and using correction factors obtained by Müller et al. (2011) without a submicron size cut-off. Uncertainties on the absorption coefficient are on the order of

30% (Müller et al., 2011). The nephelometer was calibrated with particle-free air and high-purity CO_2 prior to and after the campaign.

Prior to the campaign, the CAPS data were evaluated against the combination of the nephelometer and the PSAP measurements. The instrument intercomparison has been performed with purely scattering ammonium sulfate particles and with strongly absorbing black carbon particles. Both types of aerosols were generated by nebulizing a solution of the respective substances and size-selected using a Differential Mobility Analyzer. For instrument intercomparison purposes, the extinction coefficient from the nephelometer and PSAP was adjusted to that for 530 nm by using the scattering and absorption Angstrom exponent. The instrument evaluation showed an excellent accuracy of the CAPS measurements by comparison to the combination of nephelometer and PSAP measurements. The level of uncertainty obtained for the test aerosol was beyond the upper limit of the CAPS uncertainty which was estimated to be +-3% according to Massoli et al. (2010).

Total particle concentration for particle diameters above 10 nm (N_{10}) are made using a Condensational Particle Counter (CPC, model MARIE built by University of Mainz), calibrated prior to the experiment (sampling time 1 Hz). The associated uncertainty is on the order of 10%. Aerosol optical size in the range 0.25–25 µm is measured using an Optical Particle Counter (OPC, model 1.109 from GRIMM Technologies) in 32 channels, with a 6 s sampling rate. Particulate matter number concentrations for size ranges smaller than 1 µm, between 1 and 2.5 µm and between 2.5 and 10 µm are computed from the OPC, and are referred to N_{PM1}, $N_{PM2.5}$ and N_{PM10} respectively, in the following. The GRIMM OPC was calibrated with size-standard particles prior and after the field campaign.

Sampling with all the above mentioned instruments is achieved through the Community Aerosol Inlet of the ATR 42.

Regarding gas phase chemistry, we make use of an O_3 analyzer and a NOx analyzer from Thermo Environmental Instruments (TEI Model 49i and TEI 42CTL, respectively). The associated uncertainty is on the order of 5 and 10% respectively. Carbon monoxide (CO) measurements are performed using the near-infrared cavity ring-down spectroscopy technique (G2401, Picarro Inc., Santa Clara, CA, USA), with a time resolution of 5 s.

All in-cloud measurements are removed from the data shown here.

2.2 Space-borne observations

The Spinning Enhanced Visible and Infra-Red Imager (SEVIRI), onboard Meteosat Second Generation (MSG), measures aerosol optical depth (AOD) with spatial and temporal resolutions of 10 km and 15 min, respectively (Bennouna et al., 2009). We use the operational version 1.04 of the AOD product at 550 nm, downloaded from the ICARE data service center (http://www.icare.univ-lille1.fr/).

The Moderate Resolution Imaging Spectroradiometer (MODIS, Salmonson et al., 1989; King et al., 1992) flies aboard the polar-orbiting platforms Aqua and Terra. Terra crosses the Equator from north to south in the morning (~1030 local time), whereas Aqua crosses from south to north during the afternoon (~1330 local time). They provide a complete coverage of the Earth surface in one to two days with a resolution between 250 and 1000 m, depending on the spectral band. In the following, we use MODIS-derived level 2 AODs at 550 nm from both Terra and Aqua. Level 2 products are provided as granules with a spatial resolution of 10 km at nadir. The standard deviation on the AOD retrieval (Remer et al., 2005) over land (ocean) is $0.15\pm0.05\times\mathrm{AOD}$ ($0.05\pm0.03\times\mathrm{AOD}$). We also use level 3 daily sea surface temperature (SST) data derived from the 11 µm thermal infrared band available at 9.26 km spatial resolution for daytime passes (Werdell et al., 2013).

The hourly land surface temperature products from the Copernicus Global Land Service (https://land.copernicus.eu/global/products/lst) used in this study are available at 5 km spatial resolution. The radiative skin temperature of the land surface is estimated from the infrared spectral channels of sensors onboard a constellation of geostationary satellites (among which SEVIRI on MSG). Its estimation further depends on the surface albedo, the vegetation cover and the soil moisture.

Code de champ modifié

The Cloud-Aerosol LIdar with Orthogonal Polarization (CALIOP) flies onboard the Cloud-Aerosol Lidar Pathfinder Satellite Observation (CALIPSO), following a similar polar orbit than Aqua within the A-train constellation. In this work, we use CALIOP level-2 data (version 4.10) below 8 km above mean sea level (amsl; https://www-calipso.larc.nasa.gov/products/). Details on the CALIOP instrument, data acquisition and science products are given by Winker et al. (2007). We mainly consider the aerosol typing, which was corrected in version 4.10, as described in Burton et al. (2015).

2.3 Radiosounding network

During the DACCIWA field campaign, the upper air network was successfully augmented in June and July 2016 to a spatial density unprecedented for SWA (see Flamant et al., 2018). In this study, we use radiosounding data from meteorological balloons launched in Abidjan, Accra and Cotonou in the afternoon of 2 July (see **Figure 1**). The management of soundings at Abidjan and Cotonou was subcontracted to a private company, while the Ghana Meteorological Agency took care of the soundings in Accra. The Karlsruhe Institute of Technology was instrumental in the Ghana sounding and staff from the Agence pour la Sécurité de la Navigation Aérienne en Afrique et à Madagascar helped with the Abidjan and Cotonou soundings.

3. Models and simulations

3.1 ECMWF operational analyses & CAMS forecasts

For the investigation of atmospheric dynamics at the regional scale, we use operational analyses from the Integrated Forecasting System (IFS, a global data assimilation and forecasting system) developed by the European Centre for Medium-Range Weather Forecasts (ECMWF). The analyses presented in this paper are associated with IFS model cycle CY41r2. The original $T_{CO}1279$ (O1280) resolution of the operational analysis was transformed onto a 0.125° regular latitude-longitude grid. Long-range transport of biomass burning and dust laden air masses transported over the Gulf of Guinea are monitored with respective optical depths at 550 nm calculated from the ECMWF Copernicus Atmosphere Monitoring Service-Integrated Forecasting System (CAMS-IFS; Flemming et al., 2015) available at a resolution of 0.4°.

3.2 WRF and CHIMERE simulations

The WRF model (version v3.7.1, Shamarock and Klemp, 2008) and the CHIMERE chemistry-transport model (2017 version, Mailler et al., 2017) are used in this study. WRF calculates meteorological fields that are then used in off-line mode by CHIMERE to (i) conduct tracer experiments and (ii) compute backplumes. WRF and CHIMERE simulations are performed on common domains. For the period 30 June–-3 July 2016, two simulations are conducted for both WRF and CHIMERE to provide insights into the airborne observations: a simulation with a 10-km mesh size in a domain extending from 1°S to 14°N and from 11°W to 11°E (larger than the domain shown in **Figure 1a**) and a simulation with a 2-km mesh size in a domain extending from 2.8°N to 9.3°N and from 2.8°W to 3.3°E (**Figure 1a**).

The nested WRF simulations are first performed with hourly outputs. For the two horizontal resolutions, the same physical parameterizations are used and are those described in Deroubaix et al. (2018). The ABL scheme is the one proposed by the Yonsei University (Hong et al., 2006), the microphysics is calculated using the Single Moment-6 class scheme (Hong and Lim, 2006), the radiation scheme is RRTMG (Mlawer et al., 1997), the cumulus parameterization is the Grell-Dévényi scheme and the surface fluxes are calculated using the Noah scheme (Ek et al., 2003). The 10-km WRF simulation uses National Centers for Environmental Prediction (NCEP) Final global analyses as initial and boundary conditions. NCEP Real-Time Global SSTs (Thiébaux et al., 2003) are used as lower boundary conditions over the ocean. The meteorological initial and boundary conditions for the 2-km WRF simulation are provided by the 10-km WRF run, which, in turn, receives information from the 2-km WRF simulation (two-way nesting). The chemistry and aerosol initial and boundary conditions for the 2-km CHIMERE simulation are provided by the 10-km simulation (one-way nesting). The simulations are carried out using 32 vertical sigma-pressure levels from the surface to 50 hPa, with 6 to 8 levels in the ABL.

Then the CHIMERE simulations are performed. The horizontal grid is the same as WRF. Vertically, CHIMERE uses 20 levels from the surface to 300h Pa and three-dimensional meteorological fields are vertically interpolated from the WRF to the CHIMERE grid. The two-dimensional fields, such as 10-m wind speed, 2-m temperature, surface fluxes and boundary-layer height are used directly in CHIMERE. The chemistry and aerosol initial and boundary conditions for the 2-km CHIMERE simulation are provided by the 10-km simulation (one-way nesting). ~~for WRF and with 20 levels from the surface to 300hPa for CHIMERE. This model configuration is the same as described in Deroubaix et al. (2018).~~

The representation of the atmospheric dynamics in the 2-km simulation was verified against dynamical and thermodynamical observations from both aircraft (**Figure S1**) and the DACCIWA radiosounding network from Accra and Cotonou (**Figure S2**), yielding satisfactory results. For each aircraft and sounding data point, the corresponding WRF grid cell value is extracted. A bilinear interpolation is performed horizontally to exactly match the horizontal position of the balloon or aircraft. Linear interpolations are also performed vertically between two WRF levels as well as temporally between two consecutive model outputs to match the altitude of the balloon or aircraft at the time the pressure, temperature, humidity and wind observations are made.

3.2.1 Tracer experiments

A series of numerical tracer experiments were conducted to aid interpreting airborne observations, particularly by separating (locally emitted) urban pollution from long-range transported aerosol plumes. Passive tracers were set to be released from four major coastal cities: Accra (Ghana, 5.60°N, 0.19°W), Lomé (Togo, 6.17°N, 1.23°E), Cotonou (Benin, 6.36°N, 2.38°E) and Lagos (Nigeria, 6.49°N, 3.36°E). We conducted two sets of experiments: one for which emissions from the cities are identical (TRA_I, with "I" standing for "identical") and one for which the emissions are different and proportional to the size of the population (TRA_D, with "D" standing for "different"), based on the World Urbanization Prospect report (2015). In the latter case, emissions from Lomé, Accra and Lagos are scaled to Cotonou emissions (1.8, 3 and 13 times, respectively). Large cities in developing countries are generally considered to generate an atmospheric pollution roughly proportional to their total population due to a lack of adequate emission policies. Tracers are emitted in the lowest level of the model (below 10 m altitude) during the period of interest: in experiences TRA_D12 and TRA_I12, tracers are emitted continuously on 1 and 2 July, while in experiences TRA_D1~~2~~ and TRA_D2~~3~~, tracer emissions only occur on 1 July and 2 July, respectively. Emissions take place in a 2 km x 2 km mesh for each city. For the sake of simplicity, emissions are constant in time and thus do not have a diurnal cycle. Tracer concentrations in the atmosphere are then shown in arbitrary units (a.u.) and colored according to the city: blue for Accra, green for Lomé and red for Cotonou.~~ By design, the lifetime of the tracers emitted at a given time from any of the considered cities is 48h. After that time, tracers have either moved out of the domain or their concentration is set to zero.~~

3.2.2 Backplumes

Backplumes (or back trajectory ensembles) are computed according to Mailler et al. (2016), using a dedicated regional CHIMERE simulation with a mesh size of 30 km, covering the whole of Africa. The objective is to assess the origin of an elevated aerosol layer observed with the lidar ULICE (see Section 5). For this study, 50 tracers are released at the same time for selected locations along the ATR 42 flight trajectory, where large aerosol contents are observed: (i) the southernmost part of the flight (2.0°W, 4.5°N) and (ii) the northernmost part of the flight (1.0°E, 5.5°N). For both locations, backplumes are launched at 2500 m ~~above sea level~~amsl on 2 July 2016 at 17:00 UTC (i.e. the height of the elevated aerosol layer above the Gulf of Guinea, see Section 5). Very similar results are obtained for both backplumes. A similar sensitivity analysis is conducted by changing the altitude of the backplume from 2500 m to 3500 m amsl, but the effect is small (not shown). There again, very similar results are obtained for both backplumes. Hence, in the following we shall only show results from the backplume released from the northernmost location at 2500 m amsl.

Mis en forme : Couleur de police : Automatique

Mis en forme : Couleur de police : Automatique

4. Synoptic situation and airborne operations on 2 July 2016

The entire DACCIWA aircraft campaign took place during WAM post-onset conditions (Knippertz et al., 2017), i.e. after the migration of the climatological precipitation maximum from the coast to the Sahel, with the monsoon flow being well established over SWA. The campaign ~~also~~ took place after the onset of the Atlantic Cold Tongue as evident in Figure 3 of Knippertz et al. (2017), which also highlights that the coastal upwelling started progressively building up around 27 June 2016.

In the period spanning from 29 June to 5 July 2016, the major weather disturbances over SWA are associated with African Easterly Waves traveling along a well-organized African Easterly Jet (AEJ). A cyclonic center propagating to the south of the AEJ (identified from ECMWF 850 hPa streamline charts, not shown) originated from eastern Nigeria on 29 June, sweeping through SWA during the following days.

On 2 July 2016, the cyclonic center is located at the coast of Sierra Leone (see disturbance labelled "F" in Fig. 14 of Knippertz et al., 2017). The monsoonal winds are almost southerly over the Gulf of Guinea (south of 4°N) and progressively veer to southwesterly farther north and over the continent (**Figure S3a**). In the mid-troposphere, SWA is under the influence of easterly flow conditions (**Figure S3b**). West of 5°E, the AEJ is located over the Sahel and is intensified along its northern boundary by a strong Saharan high located over Libya. The AEJ maximum is seen off the coast of Senegal.

The region of interest experiences high insolation on 1 July with temperatures in the 30s °C across SWA and widespread low-level clouds dissolving rapidly in the course of the morning. On 2 July, there is a clear indication of land-sea breeze clouds in the high-resolution SEVIRI image at 1200 UTC (**Figure 2a**) with relatively cloud-free conditions over the ocean, where the ATR 42 flew later on. The land-sea breeze front is seen in-land to follow the coastline from western Ghana to western Nigeria. The front is observed to move farther in-land until 1500 UTC (**Figure 2b**) with shallow convective cells forming along it. Farther south the area is free of low-level clouds (both over land and ocean). Oceanic convection occurred offshore on the previous day and mesoscale convective systems were present over north-central Nigeria in the morning of 2 July. Satellite images show both oceanic and inland convection to be decaying by midday (**Figure 2a**).

On 2 July, the ATR 42 aircraft took off from Lomé at 1445 UTC (*NB: UTC equals local time in July in Togo*) and headed towards the ocean, flying almost parallel to the Ghana coastline (**Figure 1a**) at low level (in the marine ABL). Before reaching the Cape Three Points (close to the border between Ghana and Ivory Coast), the ATR 42 changed direction and headed south. Upon reaching its southernmost position (~3°N), the ATR 42 turned around and climbed to 3200 m amsl and finally headed back to Lomé at that level. On the way back, the aircraft changed heading around 1653 UTC to fly along the coast prior to landing. The ATR 42 passed the longitude of Accra at 1729 UTC and landed in Lomé at 1807 UTC. The high-level flight back allowed mapping out the vertical distribution of aerosols and clouds using the lidar ULICE. In situ aerosol and gas phase chemistry measurements will be used in the following to characterize the composition of aerosols and related air masses sampled with the lidar, particularly during the ascent over the ocean (between 1633 and 1647 UTC), the elevated leveled run and the descent towards the Lomé airport (between 1753 and 1807 UTC).

5. Atmospheric composition over the Gulf of Guinea and the link with lower tropospheric circulation

Figure 3 shows ULICE-derived ASR and VDR cross-sections acquired between 1640 UTC and 1800 UTC, including data gathered during the aircraft ascent over the ocean and descent in the vicinity of the coast. It is worth noting that most of the lidar data shown in **Figure 3** were acquired while the aircraft was flying along the coastline (from 1653 UTC on). Wind measurements from the Abidjan, Accra and Cotonou soundings as well as from the ATR 42 sounding over the ocean clearly show that above 1.2 km amsl the flow is easterly over the region of aircraft operation (**Figure 4**). Given that the heading of the aircraft along this elevated leg is 65°, the lidar "curtains" above 1.2 km amsl in **Figure 3** are mapping out aerosol layers that are transported westward (with the ATR 42 flying against the mean flow).

Several outstanding features are highlighted in **Figure 3**. Generally few clouds were encountered along the flight track (they appear in dark red colors). Exceptions are the low-level clouds at the top of the marine ABL with a base around 500 m amsl to the west of the track between 1655 and 1702 UTC (**Figure 3a**). The vertical extension and the number of the cumulus clouds topping the marine ABL decreases towards the east. This shoaling of the marine ABL is likely ascribed to the increasing trajectory length of near-surface parcels over the cold coastal waters (as the aircraft flies over the coastal upwelling region). Near Lomé, the top of the marine ABL can only be identified from the higher ASR values reflecting the impact of high relative humidity on the scattering properties of the marine aerosols (**Figure 3a**). An isolated deeper convective cloud is observed before 1648 UTC between 2 and 2.5 km, which is also sampled in situ by the ATR 42 cloud probes. The top of the cloud is likely connected to a temperature inversion observed during the aircraft ascent over the ocean (not shown). High lidar-derived ASRs are observed near the marine ABL top and to some extent in the mixed layer (**Figure 3a**). The ASR-enhanced layers do not show on the VDR plot, ~~P~~possibly because they are related to the presence sea-salt aerosols which are spherical particles that do not depolarize the backscattered lidar signal. However, the high ASR values could also be related to the advection of biomass burning aerosols from the south in the marine ABL (e.g. Menut et al., 2018) as suggested by the relatively high CO and extinction coefficient values observed in the ABL over the ocean (110 ppb and 50 Mm^{-1}, respectively) in Figure 54c and 54e. Biomass burning aerosols are also generally associated with low VDR values.

In addition to clouds and marine ABL aerosols, several distinct aerosol features in the free troposphere stand out from the lidar plot:

- **Features A and B** correspond to plumes with high values of ASR (larger than 1.2) and VDR (larger than 0.8%) observed near the coast between the surface and 0.5 km amsl and between 0.5 and 1.5 km amsl, respectively, during the aircraft descent towards Lomé. According to the aircraft in situ observations, feature B is located in a strong wind shear environment at the top (~600 m) of the ABL (**Figure 4**) with its upper part being located in the easterly flow, while feature A is associated with a south-southwesterly flow. This sheared environment likely explains the slanted structure of the aerosol plume associated with feature B.
- **Feature C** is an intermediate aerosol layer characterized by VDR values lower than those for feature B, suggesting more spherical (possibly more aged pollution) aerosols. This feature is bounded by much lower VDR values, especially above, while being associated with higher ASR values than its immediate environment. This feature is slanted between Lomé and the deeper isolated cloud. The layer thickness is larger near Lomé than over the more remote ocean, leading to a less slanted layer top. This layer has also been sampled in situ by the ATR 42 during its ascent over the ocean. It is characterized by VDRs on the order of 0.7%. Based on the aircraft sounding data, it appears that this layer is mostly advected with the easterly flow above 1.2 km amsl (**Figure 4**).
- **Feature D** is an elevated aerosol layer observed at the level of the aircraft (i.e. at 3200 m amsl) in the vicinity of Lomé, which was also sampled in situ by the ATR 42.

This layer is separated from feature B by a ~500 m deep layer of non-depolarizing aerosols (very low VDRs). The base of this layer exhibits a slanting similar to the one observed for the top of the intermediate aerosol layer (feature B). Large VDRs are found in the core of this feature (> 1.2%). It appears that this layer is also advected with the easterly flow above 1.2 km amsl.

- **Feature E** is also an elevated aerosol layer, but observed farther south over the ocean and in the vicinity of the isolated deeper cloud. It is characterized by large ASR values but low VDR values (suggesting the presence of low-depolarizing aerosols).

Given the distance of the oceanic profile to the coast (~100 km), we consider the oceanic (ascending) profile as representative of background aerosol/gas phase conditions upstream of coastal SWA. Using this profile as reference, we have analyzed the characteristics of the aerosol plume sampled with the ATR 42 (both in situ and remotely) during the aircraft descent over Lomé. The most significant differences between the ATR 42 observations acquired during the oceanic profile and the profile over Lomé are found below 1.7 km amsl (**Figure 5**) and are associated with features A and B.

ATR 42 observations associated with feature A (below 0.5 km amsl) show increases in NO_x, CO and PM1 aerosol concentrations (**Figure 5a, c, f**, respectively) as well as extinction coefficient (**Figure 5e**), together with an O_3 concentration reduction (**Figure 5b**). Plume A is related to fresh anthropogenic emissions from Lomé, including NO_x. The addition of a large quantity of NO_x into the atmosphere can lead to a significant shift in the ozone chemical equilibrium, which can effectively result in near-source consumption, as observed here. No CPC-derived aerosol concentrations are available below 0.5 km amsl. The few PSAP measurements made around 0.5 km amsl during the descent yield an AAE value around ~1 (**Figure 5g**). ~~Furthermore, the ratio of O_3 to CO concentrations is on the order of 0.15 (not shown).~~ These are solid indications that the ATR 42 sampled a fresh urban anthropogenic plume near Lomé (Brito et al., 2018), advected with the south-southwesterly monsoon flow (the ATR 42 being downstream of Lomé then).

ATR 42 observations associated with feature B (between 0.5 and 1.5 km amsl) show increases in concentrations for all variables under scrutiny, including O_3. The latter (**Figure 5b**) is the most significant difference between the characteristics of features B and A. Other differences include the much smaller increases in CO concentration and OPC aerosol (N_{PM1}, $N_{PM2.5}$ and N_{PM10}) concentrations as well as extinction coefficients observed in feature B (**Figure 5c, e, f**, respectively). The O_3/CO ratio (an indicator of air mass aging, e.g. Jaffe and Wigder (2012) and Kim et al. (2013)) observed to be associated with feature B increases with respect to feature A (0.25 vs. 0.15, i.e. a 65% increase), which is compatible with a further processed urban plume, as also corroborated by wind measurements. ~~The O_3/CO ratio is also larger (i.e. 0.25, not shown) than that associate with feature A.~~ These observations, together with wind measurements, suggest that feature B corresponds to a more aged urban plume. This could be an indication that the ATR 42 sampled more than just the Lomé plume. This will be investigated using tracer experiments in Section 6. Above 2 km amsl, the AAE increases to larger values (> 1.5), evidencing a change in aerosol nature, i.e. a transition from local urban emissions to elevated background pollution (**Figure 5g**), possibly resulting from a mixture of long-lived anthropogenic pollution and long-range transport of dust and biomass burning aerosols from previous days.

Regarding feature C, the in situ measurements do not allow characterizing the nature of the aerosols. The origin of this layer will also be investigated using tracer experiments (see Section 6).

The in situ measurements along the elevated ATR 42 track reveal significant differences in aerosol/gas phase concentrations and properties between the western part (where feature E is observed with the lidar) and the eastern part (where feature D is observed) of the ATR 42 leg (**Figure 6**). In the western part, ATR 42 measurements highlight enhanced O_3 and CO concentrations (> 60 ppbv and > 200 ppvb, respectively, **Figure 6a, b**) together with AAE values of ~1.5 (**Figure 6f**), suggesting the presence of biomass burning aerosol. Furthermore, aerosol number concentrations N_{PM1} and N_{10} show enhanced values for small particles (100 # cm^{-3} and ~1000 # cm^{-3}, respectively, **Figure 6c, d**). The observed O_3, CO and N_{10} concentrations are larger than the background values measured during the ascent over the ocean (~40 ppbv, 150 ppbv, and 500 # cm^{-3}, respectively, **Figure 5b, c, f**). Large extinction values are also observed (100 Mm^{-1}), largely exceeding the background value of 30 Mm^{-1}(compare **Figure 6e and Figure 5e).**

In the eastern part of the leg, AAE values of ~1.5 also suggest that biomass burning aerosols are sampled. O3, CO, N_{PM1} and N_{10} concentrations diminish approximately half way through the leg to their background values (from 1716 UTC on, **Figure 6a, b, c, d**), as does the extinction coefficient. However, $N_{PM2.5}$ and N_{PM10} concentrations increase significantly, as opposed to N_{PM1}, which combined with enhanced lidar-derived VDR suggest mixing with larger particles, possibly dust. Further insight into the origin of these aerosols, observed as a result of long-range transport, will be investigated in Section 7.

Finally, in Section 8 we will investigate the cause of the slanting of the elevated aerosol layers from west to east along the flight track, which also possibly leads, in addition to the colder SSTs, to a thinning of the marine ABL and the suppression of clouds at its top in the vicinity of Lomé (**Figure 3**).

6. Tracer experiments for anthropogenic aerosols

The objectives of the tracer experiments are threefold: (i) understand how the lower tropospheric circulation shapes the structure of the urban pollution plume emitted from coastal cities and observed with the ULICE lidar (marked A and B in **Figure 3**), (ii) assess which cities contribute to the plume observed with ULICE and whether it results from Lomé emissions only, and (iii) provide insight into the origin of the intermediate aerosol layer (marked B in **Figure 3**). For this we have analyzed along the ATR 42 aircraft flight track the tracer simulations introduced in Section 3.

As an ancillary objective, we also aim to assess how far over the ocean the urban pollution aerosols can be transported by the complex low-level circulation over SWA. For this, we have analyzed the tracer simulations along four 0.5°-wide north–south transects spanning the longitudinal range of the ATR 42 flight (centered at 0.75°W, 0.25°W, 0.25°E and 0.75°E, cf. **Figure 1b**).

6.1 Structure of the urban plume along the coastline

Figure 7 shows the structure of the urban pollution plume along the aircraft track between 1400 and 1800 UTC in the TRA_D and TRA_I experiments. In TRA_D12 (**Figure**

7a), feature A as observed in the lidar VDR field (**Figure 3**) corresponds to emissions from Lomé only (in greenish colors) in the ABL (~~blue~~ magenta dotted line), while feature B corresponds to emissions from Lomé mainly with a contribution from Accra (superimposed with the Lomé plume) and Cotonou (reddish colors in the upper western boundary of the Lomé plume). In the TRA_I12 experiment, the Accra contribution is missing altogether (**Figure 7b**). More strikingly, TRA_D2~~1~~ shows an elevated tracer plume over the ocean originating from Accra (blueish colors), which mimics feature C in **Figure 3** fairly well. This feature is almost absent in TRA_I1, stressing the importance of accounting for enhanced emissions from Accra (with respect to Lomé and Cotonou) to produce a more realistic tracer simulation.

Results from experiment TRA_D1~~2~~ (**Figure 7c**) shows that feature C in the lidar VDR observations is likely related to emissions from Accra from the previous day only (i.e. 1 July), as the structure of the Accra plume in TRA_D12 and TRA_D1~~2~~ is the same. In ~~this~~ experiment TRA_D1, the structures of the plume corresponding to features A and B in **Figure 3** are clearly altered by the lack of recent emissions in Lomé on 2 July (the lower part of the plume is likely advected northward with the southerly flow here). This is confirmed by looking at the result of TRA_D2~~3~~ (**Figure 7d**): the fresh emissions (on 2 July) from Lomé do lead to a realistic simulation of the shape of features A and B observed by lidar. On the other hand, feature C is not reproduced in this experiment, suggesting that feature B as observed by lidar is a mix of fresh and more aged emissions from Lomé, as well as aged emissions from Cotonou and Accra, while feature C is almost entirely related to aged pollution from Accra. What is also worth noting is that no emissions from Lagos on 1 and 2 July are observed along the ATR 42 flight track in the TRA_D and TRA_I experiments.

6.2 Southward transport of the urban plume over the Gulf of Guinea

Figure 8 shows the structure of the urban pollution plume along four 0.5°-wide north–south transects centered at 0.75°W, 0.25°W, 0.25°E and 0.75°E on 2 July at 1600 UTC, i.e. half way through the ATR 42 flight.

Along the westernmost transect, labeled I in **Figure 1b** (centered at 0.75°W), the pollution plume is only composed of emissions from Accra and is lifted off the surface above the ABL (**Figure 8a**). Note that no tracer emissions directly occur in this transect, with Accra emissions being contained in transect II, to the east of transect I. As discussed by Knippertz et al. (2017), during the campaign, pollution plumes from coastal cities were mostly directed northeastwards (see their Figure 19). Hence the tracer plume seen in the experiment on 2 July is associated with transport of tracers emitted on 1 July in the monsoon flow toward the northeast, which are then vertically mixed (due to thermally and mechanically driven turbulence), and westward advection of the tracers by the easterly flow above the monsoon layer. Over the ocean, the plume is seen to extend as far south as 4.7°N, i.e. the southernmost extension seen on all transects shown in **Figure 8**. This is linked to a small equatorward component in the easterly flow~~ (not a meridional overturning circulation)~~.

Along the transect centered at 0.25°W (transect II, **Figure 1b**), the plume is seen to be in contact with the surface as far north as 6.5°N (**Figure 8b**). The strong ascent at 6°N is related to the presence of the Mampong range in the Ashanti uplands (see **Figure 1b**). The presence of the range and the associated upward motion contributes to deep mixing of the plume north of Accra with the top of the tracer plume reaching 4 km above the ground level or higher. Strong subsidence is seen north of the

Mampong range that mixes tracers down to the surface. Other ascending and subsiding motions are detectable over the Lake Volta area, which could be related to land-lake breeze systems. South of 6°N, the tracer plume is as deep as along transect I, but does not extend southward over the ocean. Here also, only emissions from Lomé contribute to the pollution plume on 2 July, suggesting that it took 24 h for these emissions to reach transect II.

The pollution plume along the transect centered at 0.25°E (transect III) is structurally similar to the one along transect II, but reaches farther inland (~7.5°N at the surface, **Figure 8c**) than in transect II, likely due to the gap between the Mampong range and the Akwapim-Togo range, and the flat terrain around Lake Volta. Again, ascending and subsiding motions are detectable over the Lake Volta area that could be related to land-lake breeze systems. Over the ocean, the plume reaches 5.3°N at 1.5 km amsl. Emissions from Lomé and Cotonou contribute to the upper and southernmost part of the tracer plume along this transect, just north of 5.6°N.

Finally, along transect IV, the composition of the urban pollution plume is dominated by emissions from Accra, with a small contribution of emissions from Cotonou and Lomé in the southern, uppermost part of the plume because of short-range westward transport above the monsoon flow (**Figure 8d**). The Accra plume is seen to extend from the coastline to as far as 9°N and above the depth of the continental ABL, but not as deep as along other transects with more pronounced orography. The northward extension of the plume suggests that emissions from Accra are transported over Togo along the eastern flank of the Akwapim-Togo range. Over the ocean, the upper part of the plume barely reaches 5.6°N at an altitude of 2 km amsl.

The differences seen in the structure of the pollution plume obtained from the tracer experiment over land are likely due to interactions between the monsoon flow and the orography just to the north of Accra: namely the southeast–northwest running Mampong range and the north-south running Akwapim-Togo range to the east of Accra, both bordering Lake Volta (**Figure 1b**). In addition to those orographic effects, the monsoon flow transporting the tracers towards the north may also interact with the land-lake breeze system occurring in the summer over Lake Volta (Buchholz et al., 2017a, b). Addressing the impact of these complex circulations over land on the urban pollution plumes is beyond the scope of this paper.

Strikingly, as in the along aircraft flight track cross-section, emissions from Lagos on 1 and 2 July are never seen in the north-south transects, confirming that they likely do not impact on the air quality in the major coastal cities to the west during this period. Furthermore, the tracer simulations suggest that the pollution plume over SWA related to emissions in the four cities considered here does not extend very far over the ocean (to 4.7°N at most), essentially because they are transported northward within and westward above the marine ABL. Nevertheless, the western part of the Accra pollution plume spreads farther south over the ocean than the eastern part.

7. Long-range transport of aerosols related to regional-scale dynamics

To gain insights into the origin of the aerosol layers sampled by the ATR along the elevated leg and observed by lidar (features D and E in **Figure 3**), 10-day back-trajectories ending at 2500 m amsl at 1700 UTC on 2 July are computed using CHIMERE. The backplume associated with feature D is shown in **Figure 9a** (the one associated with feature E is nearly identical and will not be discussed). The back trajectories suggest that feature D originates from a broad area including Gabon, Congo and the Democratic Republic of Congo. Most of the back trajectories then travel over the Gulf of Guinea towards SWA in the free troposphere (**Figure 9b**). Daily mean AOD derived from MODIS and SEVERI observations on 2 July (**Figure 10a**) show large values offshore of Gabon and Congo known to be biomass burning aerosol emission hotspots at this time of year (e.g. Menut et al., 2018). This is corroborated by the CAMS biomass burning aerosol forecast at 1200 UTC (**Figure S4a**).

The afternoon CALIOP observations acquired to the east of the ATR 42 flight track across the enhanced AOD feature (see track in **Figure 10a**) indeed classify the aerosols over the ocean as elevated smoke, transported between 1.5 and 4 km amsl (**Figure 10b**). The altitude of transport is consistent with that derived from the CHIMERE backplume (**Figure 9b**) as also shown by Menut et al. (2018). Along this transect, dust is observed to almost reach the SWA coastline from the north (**Figure 10b**) consistent with the moderate AOD values observed over Togo and Benin (**Figure 10a**). Furthermore, the morning ATR 42 flight conducted on 2 July in the region of Savè (Benin, ~8°N) highlighted the presence of dust over northern Benin (Flamant et al., 2018). Interestingly, at the coast (~6°N), CALIOP shows evidence of polluted dust, possibly resulting from the mixing of dust with anthropogenic emissions from coastal cities. However, the CAMS forecast does not show dust reaching the SWA coast (**Figure S4b**).

The backplume and regional scale dynamics analyses indicate that the upper-level aerosol features D and E (as observed by lidar) are related to biomass burning over Central Africa. In the case of feature D, closer to Lomé, MODIS, SEVIRI and CALIOP observations suggest the possibility of mixing with dust, which is consistent~~ly~~ with the ATR in situ and lidar-related observations.

8. Coastal circulations: the role of surface temperature gradients and orography

IFS vertical velocity computed between 850 and 600 hPa (i.e. above the monsoon flow) shows that most of the northern Gulf of Guinea is under the influence of subsiding motion on 2 July at 1800 UTC (**Figure 11b**). Stronger subsidence is seen to the east of the region of operation of the ATR 42 at that time. Strong subsidence is also seen over the eastern part of the ATR 42 flight track at 1200 UTC (**Figure 11a**). However, at 1200 UTC, the eastern part of the northern Gulf of Guinea is characterized by upward motion, possibly in relationship with the SST gradient (cold water to the west linked with the coastal upwelling and warmer waters to the east in the Niger delta region). The signature of the sea breeze is also visible inland in the IFS analysis at 1200 UTC (**Figure 11a**) in the form of a line of strong ascendance running parallel to the coastline.

At the regional scale, IFS analyses evidence the existence of marked surface temperature difference between the ocean and the continent at 1200 UTC (**Figure S5d**) because of the high insolation across SWA as noted in Section 2. The surface temperature gradient across the coast creates shallow overturning circulations as evidenced by IFS analyses at 1800 UTC (**Figure 12**). A well-defined closed zonal cell can be identified below 600 hPa around 5°N and between 0°E and 8°E (**Figure 12a**), while a well-defined meridional cell is seen around 0°E between 3°N and 8°N (**Figure 12c**). It is worth noting that the overturning circulations are most intense and better defined at 1800 UTC than at 1200 UTC (compare **Figure 12a** with **Figure S5c** for the zonal cell), even though the surface temperature difference across the coast is weaker (compare **Figure 12b** with **Figure S5d**). The overturning circulation exhibits a strong diurnal cycle (**Figure S5**), which is driven by the surface temperatures over land. The quality of IFS skin temperature during the day was verified against observed land surface temperature observations (so-called Copernicus product; see **Figure S6**). In spite of a systematic bias on the order of 2°C over land, IFS skin temperature analyses are seen to be consistent (in terms of spatio-temporal distribution) with the Copernicus product (**Figure S6**). This gives us confidence that the overturning circulations exist~~s~~ and contribute~~s~~ to enhance subsidence over the Gulf of Guinea. Furthermore, we have conducted an analysis of the correlation between the land-sea skin temperature gradients associated with both the zonal and the meridian cells and the vertical velocity over the Gulf of Guinea at different times of day for the whole of July 2016, based on IFS data (**Table 2**). The analysis shows that the zonal land-sea skin temperature gradient at 1200 and 1800 UTC is significantly correlated with vertical velocity at 1800 UTC with values around 0.5. Hence, the overturning cells evidenced on 2 July appear to be persistent features over the Gulf of Guinea, at least in post-monsoon onset conditions. On the other hand, the meridional land-sea skin temperature gradient at 1200 UTC is correlated (0.34) with vertical velocity at 1200 UTC, possibly due to the presence of orography as discussed in the following. The meridional gradient of skin temperature between the sea and the land is an indicator for the pressure difference and thus drives the intensity of the southerly flow associated with the land sea breeze. When the southerly flow impinges on the low terrain over SWA, as it progresses over the continent, enhanced vertical motion is generated. ~~Hence, the overturning cells evidenced on 2 July appear to be persistent features over the Gulf of Guinea, at least in post-monsoon onset conditions.~~

In addition to the subsidence generated at the regional scale by the land-sea temperature gradient, the interaction of the monsoon flow with the orography over Ghana and Togo is responsible for more local coastal circulations. This interaction is reflected in the vertical velocity anomaly simulated with WRF along the western- and easternmost transects in **Figure 1b** (transects I and IV, respectively). The anomalies are computed with respect to the average vertical velocity between 1°W and 1°E. **Figure 13** shows that in the region where orography is more pronounced (i.e. to the west), the vertical velocity anomaly is positive, while it is negative to the east where orography is less marked (compare **Figure 13a** and **13b**). As a result, the eastern region of ATR 42 operation on 2 July is under the influence of strong subsiding motion. This subsiding motion suppresses low-level cloudiness near Lomé and is key to the interpretation of the ATR 42 lidar observations along the track regarding the slanting of the elevated aerosol layers and, possibly, the thinning of the marine ABL towards the eastern end of the aircraft track, together with an additional effect of colder SSTs.

MODIS observations show the existence of an SST dipole across the northern part of the Gulf of Guinea (**Figure S7** and **Figure 11**), between the coastal upwelling offshore of Lomé and Accra (SSTs on the order of 26°C) and the warmer SST to the east in the Bight of Bonny (offshore Nigeria, where SST on the order of 28°C are generally observed). Even though this SST dipole may also generate a secondary circulation over the Gulf of Guinea (e.g. around 900-800 hPa and between 0 and 1°E in **Figure S5c**), it is very likely that the lower tropospheric dynamics in the region of operation of the aircraft are dominated by the monsoon dynamics to the first order and by the sea-land surface temperature gradient at the regional scale.

9. Summary and conclusions

In this study, detailed aircraft observations on 02 July 2016 and accompanying model simulations were used to analyze the distribution of aerosols over the Gulf of Guinea and its meteorological causes. We show that land-sea surface temperature gradients between the northern part of the Gulf of Guinea and the continent as well as orography over Ghana and Togo play important roles for the distribution of aerosols and gases over coastal SWA. The former creates large-scale subsidence conditions over the northern part of the Gulf of Guinea through the generation of zonal and meridional overturning circulations below 600 hPa, with the downward branch of the circulation around 0°E over the ocean. The latter generates enhanced subsidence over the eastern part of the ATR 42 operation area, near Lomé and Accra. Together this leads to a west–east tilting of the aerosol layers (that can be considered as passive tracers of the dynamics) along the flight track. The ATR 42 sampled remotely and in situ the complex aerosol layering occurring between 2.5 and 3.2 km amsl over the Gulf of Guinea as a result of long-range transport of dust (from the northeast) and biomass burning aerosol from the south (feature E in **Figure 3**) and the mixing between these (feature D).

The orography-forced circulation also has an influence on the structure of the urban pollution plumes from Accra, Lomé and Cotonou as assessed from airborne lidar measurements on 2 July and numerical passive tracer experiments using the WRF/CHIMERE models. When accounting for the relative size of the emitting cities along the coast (~2 times more emissions in Accra than in Lomé), we find that the tracer experiment designed to include emissions from 1 and 2 July is the most realistic in reproducing the lidar observations. The analysis shows that (a) the large pollution plumes observed at the coast up to 1.5 km (features A and B) are essentially related to emissions in the Lomé area from both 1 and 2 July, with a moderate contribution from Accra and Cotonou, (b) the elevated plume over the northern part of the Gulf of Guinea (feature C) is related to emissions from Accra exclusively from the day before the ATR 42 flight (i.e. 1 July) and these clearly dominate the composition of the tracer plume in the region covered by the flight track on 2 July, (c) given the general direction of the monsoon flow, Lagos emissions (taken to be 13 times that of Cotonou) do not appear to have affected the atmospheric composition ~~be a player for regions~~ west of Cotonou, where our airborne observations were gathered, ~~in the summer in post-onset conditions~~ as also shown by Deroubaix et al. (2018) ~~in the summer~~ in post-monsoon onset conditions, and (d) the tracer plumes do not extend very far over the ocean during the short period under scrutiny, mostly because they are transported northward within the marine ABL and westward above ~~the marine ABL~~it so that their extent is controlled by the equatorward component in the mostly easterly flow as modulated by synoptic-scale disturbances (Knippertz et al., 2017).

The unique combination of in situ and remote sensing observations acquired over the Gulf of Guinea during the 2 July 2016 OLACTA flight together with global and regional model simulations revealed in detail~~s~~ the impact of the complex atmospheric circulation at the coast on the aerosol composition and distribution over the northern Gulf of Guinea. We show that the western Gulf of Benin is a place favorable for subsidence in the afternoon due to 3 factors, namely cool SSTs, zonal overturning connected with the Niger Delta region and meridional overturning connected with the main West African landmass, anchored geographically at the Mampong and Akwapim-Togo ranges. We also show that the overturning cells are robust features of the atmospheric circulation over the Gulf of Guinea in July 2016. To the best of the authors' knowledge such features have not been documented in the literature to date.

Further research will be dedicated to enhance our understanding of the complex interactions between the monsoon flow and the orography north of major coastal cities as well as the land-sea and land-lake breezes, and their impact on the dispersion of pollution emissions from major coastal cities in SWA. Future research will also be conducted to assess long-term impact of the land-sea surface temperature gradient (and related shallow overturning circulation) on distribution of aerosols over the northern Gulf of Guinea.

Acknowledgements

The DACCIWA project has received funding from the European Union Seventh Framework Programme (FP7/2007-2013) under grant agreement no. 603502. The European Facility for Airborne Research (EUFAR, http://www.eufar.net/) also supported the project through the funding of the Transnational Activity project OLACTA. The Centre National d'Etudes Spatiales (CNES) provided financial support for the operation of the ULICE lidar. The personnel of the Service des Avions Français Instrumentés pour la Recherche en Environnement (SAFIRE, a joint entity of CNRS, Météo-France and CNES and operator of the ATR 42) are thanked for their support. M. Gaetani has been supported by the LABEX project funded by Agence Nationale de la Recherche (French National Research Agency, grant ANR-10-LABX-18-01). The authors would like to thank ~~T. Bourrianne and~~ B. Piguet (CNRM) and M. Ramonet (LSCE) for their support in the data acquisition and processing. The authors would also like to thank Gregor Pante (KIT) for providing IFS data, as well as Hugh Coe,

Code de champ modifié

Sophie Haslett and Johnathan Taylor (Univ. of Manchester) for helpful discussions. The authors are thankful to the two anonymous referees whose comments helped improve the overall quality of the paper. MODIS data was made available via the Geospatial Interactive Online Visualization ANd aNalysis interface (https://giovanni.gsfc.nasa.gov/giovanni/).

Data availability

The aircraft and radiosonde data used here can be accessed using the DACCIWA database at http://baobab.sedoo.fr/DACCIWA/. The tracer simulations discussed in this paper are also available on the database. An embargo period of 2 years after the upload applies. After that, external users can access the data in the same way as DACCIWA participants before that time. Before the end of the embargo period, external users can request the release of individual datasets. It is planned for DACCIWA data to get DOIs, but this has not been realized for all datasets yet.

Competing interests

The authors declare that they have no conflict of interest.

Special issue statement

This article is part of the special issue “Results of the project ‘Dynamics-aerosol-chemistry-cloud interactions in West Africa’ (DACCIWA) (ACP/AMT inter-journal SI)”. It is not associated with a conference.

Appendix A: The ULICE lidar characteristics and data processing

For the two channels of the lidar (indexed 1 and 2), the apparent backscatter coefficient (ABC, β_{app}) is given by

$$\beta_{app}{}^{1(2)}(r) = C^{1(2)} \cdot \left(\beta_m^{1(2)}(r) + \beta_a^{1(2)}(r)\right) \cdot \exp\left(-2 \cdot \int_0^r \alpha_a(r') \cdot dr'\right) \qquad \text{(A1)}$$

where β_m and $\beta_{\cancel{p}a}$ are the backscatter coefficients for the molecular and the aerosol contributions, respectively; α_a is the aerosol extinction coefficient; $C^{1(2)}$ are the instrumental constants for each channel. The total ABC is given by:

$$\beta_{app}(r) = \frac{\beta_{app}^1(r) \cdot \left(1 + VDR(r)\right)}{C^1 \cdot \left(T_1^{//} + T_1^{\perp} \cdot VDR(r)\right)} \qquad \text{(A2)}$$

Code de champ modifié

where $T_i^{//}$ and $T_i^{\perp}$ are the transmissions of the co-polarization and cross-polarization contributions of the lidar polarized plate *i*, respectively. The VDR is thus given by the equation:

$$VDR(r) \approx \frac{T_1^{//} \cdot \beta_{app}^2(r)(r)}{R_c \cdot \beta_{app}^1(r)(r)} - \left(1 - T_1^{//}\right) \cdot \left(1 - T_2^{//}\right). \qquad \text{(A3)}$$

The apparent scattering ratio (ASR, noted R_{app}) is expressed as:

$$R_{app}(r) = \beta_{app}(r) / \beta_m^{//}(r). \qquad \text{(A4)}$$

As also shown by Chazette et al. (2012), the cross-calibration coefficient $R_c = C^2/C^1$ can be assessed by normalizing the lidar signals obtained in aerosol-free conditions, assuming the molecular VDR to be equal to 0.3945% at 355 nm, following Collis and Russel (1976). The dominant error source is the characterization of the plate transmission on the optical bench, which leads to a relative error close to 8% on the VDR (Chazette et al., 2012). During the DACCIWA field campaign, all lidar measurements were conducted within aerosol layers and therefore we had to use measurements performed just before the campaign during flight tests above the Mediterranean ~~Sea~~ for assessing R_c. During the flight over the Mediterranean, the ATR 42 was flying an altitude of 6.3 km amsl, with ULICE lidar data acquired in the nadir pointing mode between 0 and 6 km amsl. The calibration was performed using lidar data acquired well above any aerosol layers, i.e. between 5 and 6 km amsl where the lidar backscatter is only sensitive to the molecular background signal.

Table A1. Summary of ULICE lidar characteristics

ULICE lidar	Characteristics
Emitter (Laser)	Quantel Centurion, diode-pumped, air cooled
	6.5 mJ, 8 ns, 100 Hz @ 354.7 nm
Laser divergence	< 0.1 mrad
Output beam	Eyesafe ~40 × 30 mm beam, tunable 0 to 40 mrad divergence with Altechna Motex expander (at $1/e^2$)
Receiver	2 channels with the cross-polarisations
Telescope	Refractive,150 mm diameter, 280 mm effective focal length
Field of view	~3 mrad
Filtering	Narrow band filters (200 pm)
Detection	Hamamatsu H10721 photo-multiplier tubes.
Detection mode	Analog
Data acquisition	12 bits, 200 MHz sampling, 2 channels NI-5124 digitizer manufactured by the National Instruments Company.
Vertical sampling	
Native	0.75 m
After data processing	15-30 m
Weight of the optical head	~20 kg
Weight of the electronics	~10 kg
Consumption	350 W at 24-28 V DC

References

Anderson, T. L., and Ogren, J. A.~~, 1998~~: Determining aerosol radiative properties using the TSI 3563 integrating nephelometer, Aerosol Sci. Tech., 29, 57–69, 1998.

Bennouna, Y. S., ~~G.~~ de Leeuw, G., ~~J.~~ Piazzola, J., and ~~J.~~ Kusmierczyk-Michulec, J.: ~~(2009),~~ Aerosol remote sensing over the ocean using MSG-SEVIRI visible images, J. Geophys. Res., 114(D23), D23203, doi:10.1029/2008JD011615, 2009.

Bergstrom, R. W., Pilewskie, P., Russell, P. B., Redemann, J., Bond, T. C., Quinn, P. K., and Sierau, B.: Spectral absorption properties of atmospheric aerosols, Atmos. Chem. Phys., 7, 5937-5943, https://doi.org/10.5194/acp-7-5937-2007, 2007.

Bond, T. C., Anderson, T. L., and Campbell, D.~~, 1999~~: Calibration and intercomparison of filter-based measurements of visible light absorption by aerosols, Aerosol Sci. Tech., 30, 582–600, 1999.

Brito, J., ~~E.~~ Freney, E., ~~P.~~ Dominutti, P., ~~A.~~ Borbon, A., ~~S.~~ Haslett, S., ~~A.~~ Batenburg, A., ~~C.~~ Schulz, C., ~~A.~~ Colomb, A., ~~R.~~ Dupuy, R., ~~C.~~ Denjean, C., ~~A.~~ Deroubaix, A., ~~H.~~ Coe, H., ~~J.~~ Schneider, J., ~~S.~~ Borrmann, S., ~~K.~~ Sellegri, K., ~~C.~~ Flamant, C., ~~P.~~ Knippertz, P., and ~~A.~~ Schwarzenboeck, A.~~, 2018~~: Assessing the role of anthropogenic and biogenic sources on PM1 over Southern West Africa using aircraft measurements, *Atmos. Chem. Phys.* 18, 757–772, 2018.

Buchholz M., ~~A. H.~~ Fink, A. H., ~~P.~~ Knippertz, P., and ~~C.~~ Yorke, C.~~, 2017a~~: Impacts of the land-lake breeze of the Volta reservoir on the diurnal cycle of cloudiness and precipitation, EGU General Assembly, Vienna, Austria, 23-28 April 2017, 2017a.

Buchholz M. A.~~, 2017b~~: The influence of Lake Volta on weather and climate, Karlsruhe Institute of Technology Master Thesis (in German), available from http://www.imk-tro.kit.edu/download/Masterarbeit_Marcel_Buchholz.pdf, 2017b.

Burton, S. P., ~~J. W.~~ Hair, J. W., ~~M.~~ Kahnert, M., ~~R. A.~~ Ferrare, R. A., ~~C. A.~~ Hostetler, C. A., ~~A. L.~~ Cook, A. L., ~~D. B.~~ Harper, D. B., ~~T. A.~~ Berkoff, T. A., ~~S. T.~~ Seaman, S. T., ~~J. E.~~ Collins, J. E., ~~M. A.~~ Fenn, M. A., and ~~R. R.~~ Rogers, R. R.~~ 2015~~: Observations of the spectral dependence of linear particle depolarization ratio of aerosols using NASA Langley airborne High Spectral Resolution Lidar, Atmos. Chem. Phys., 15(23), 13453–13473, doi:10.5194/acp-15-13453-2015, 2015.

Carslaw, K. S., Boucher, O., Spracklen, D. V., Mann, G. W., Rae, J. G. L., Woodward, S., and Kulmala, M.: A review of natural aerosol interactions and feedbacks within the Earth system, Atmos. Chem. Phys., 10, 1701-1737, doi:10.5194/acp-10-1701-2010, 2010.

Clarke, A., McNaughton, C., Kapustin, V., Shinozuka, Y., Howell, S., Dibb, J., Zhou, J., Anderson, B., Brekhovskikh, V., Turner, H., and Pinkerton, M.~~, 207~~: Biomass Burning and Pollution Aerosol over North America: Organic Components and their influence on Spectral Optical Properties and Humidification Response, J. Geophys. Res., 112, D12S18, doi:10.1029/2006JD007777, 2007.

Chazette, P., ~~A.~~ Dabas, A., ~~J.~~ Sanak, J., ~~M.~~ Lardier, M., and ~~P.~~ Royer, P.~~, 2012~~: French

Code de champ modifié

airborne lidar measurements for Eyjafjallajökull ash plume survey, *Atmos. Chem. Phys.*, *12*(15), 7059–7072, doi:10.5194/acp-12-7059-2012, 2012.

Collaud Coen, M., Weingartner, E., Schaub, D., Hueglin, C., Corrigan, C., Henning, S., Schikowski, M., and Baltensperger, U.~~, 2004~~: Saharan dust events at the Jungfraujoch: Detection by wavelength dependence of the single scattering albedo and first climatology analysis, Atmos. Chem. Phys., 4, 2465–2480, 2004.

Collis, R. T. H., and ~~P. B.~~ Russell, P. B.~~1976~~: Lidar measurement of particles and gases by elastic backscattering and differential absorption in Laser Monitoring of the Atmosphere, edited by: Hinkley, E. D., pp. 71–152, Springler-Verlag, New York, 1976.

Deroubaix, A., Flamant, C., Menut, L., Siour, G., Mailler, S., Turquety, S., Briant, R., Khvorostyanov, D., and Crumeyrolle, S.~~, 2018~~: Interactions of Atmospheric Gases and Aerosols with the Monsoon Dynamics over the Sudano-Guinean region during AMMA, Atmos. Chem. Phys., 18, 445-465, doi:10.5194/acp-2017-552, 2018~~accepted~~

Ek, M. B., Mitchell, K. E., Lin, Y., Rogers, E., Grunmann, P., Koren, V., Gayno, G., and Tarpley, J. D.: Implementation of Noah land surface model advances in the National Centers for Environmental Prediction operational mesoscale Eta model, J. Geophys. Res.-Atmos., 108, 8851, 2003.

Evan, A. T., Vimont, D. J., Heidinger, A. K., Kossin, J. P. & Bennartz, R.~~, 2009~~: The role of aerosols in the evolution of tropical North Atlantic Ocean temperature anomalies. Science 324, 778–781, 2009.

Flamant C., ~~P.~~ Knippertz, P., ~~A. H.~~ Fink, A. H., ~~A.~~ Akpo, A., ~~B.~~ Brooks, B., ~~C. J.~~ Chiu, C. J., ~~H.~~ Coe, H., ~~S.~~ Danuor, S., ~~M.~~ Evans, M., ~~O.~~ Jegede, O., ~~N.~~ Kalthoff, N., ~~A.~~ Konaré, A., ~~C.~~ Liousse, C., ~~F.~~ Lohou, F., ~~C.~~ Mari, C., ~~H.~~ Schlager, H., ~~A.~~ Schwarzenboeck, A., ~~B.~~ Adler, B., ~~L.~~ Amekudzi, L., ~~J.~~ Aryee, J., ~~M.~~ Ayoola, M., ~~A. M.~~ Batenburg, A. M., ~~G.~~ Bessardon, G., ~~S.~~ Borrmann, S., ~~J.~~ Brito, J., ~~K.~~ Bower, K., ~~F.~~ Burnet, F., ~~V.~~ Catoire, V., ~~A.~~ Colomb, A., ~~C.~~ Denjean, C., ~~K.~~ Fosu-Amankwah, K., ~~P. G.~~ Hill, P. G., ~~J.~~ Lee, J., ~~M.~~ Lothon, M., ~~M.~~ Maranan, M., ~~J.~~ Marsham, J., ~~R.~~ Meynadier, R., ~~J.-B.~~ Ngamini, J.-B., ~~P.~~ Rosenberg, P., ~~D.~~ Sauer, D., ~~V.~~ Smith, V., ~~G.~~ Stratmann, G., ~~J. W.~~ Taylor, J. W., ~~C.~~ Voigt, C., and ~~V.~~ Yoboué, V. ~~2018~~: The Dynamics-Aerosol-Chemistry-Cloud Interactions in West Africa field campaign: Overview and research highlights, Bull. Amer. Meteorol. Soc., 99, 83-104, doi:10.1175/BAMS-D-16-0256.1, 2018.

Flemming, J., Huijnen, V., Arteta, J., Bechtold, P., Beljaars, A. Blechschmidt, A.-M., Diamantakis, M., Engelen, R. J., Gaudel, A., Inness, A., Jones, L., Josse, B., Katragkou, E., Marecal, V., Peuch, V.-H., Richter, A., Schultz, M. G., Stein, O., and Tsikerdekis, A.~~, 2015~~: Tropospheric chemistry in the Integrated Forecasting System of ECMWF, Geosci. Model Dev., 8, 975-1003, doi:10.5194/gmd-8-975-2015, 2015.

Haywood, J., and Boucher, O.: Estimates of the direct and indirect radiative forcing due to tropospheric aerosols: A review, Rev. Geophys., 38, 513–543, 2000.

Hong, S., and Lim, J.: The WRF single-moment 6-class microphysics scheme (WSM6), 42, 129–151, 2006.

Code de champ modifié ... [1]
Code de champ modifié ... [2]
Code de champ modifié ... [3]
Code de champ modifié ... [4]
Code de champ modifié ... [5]
Code de champ modifié ... [6]
Code de champ modifié ... [7]
Code de champ modifié ... [8]
Code de champ modifié ... [9]
Code de champ modifié ... [10]
Code de champ modifié ... [11]
Code de champ modifié ... [12]
Code de champ modifié ... [13]
Code de champ modifié ... [14]
Code de champ modifié ... [15]
Code de champ modifié ... [16]
Code de champ modifié ... [17]
Code de champ modifié ... [18]
Code de champ modifié ... [19]
Code de champ modifié ... [20]
Code de champ modifié ... [21]
Code de champ modifié ... [22]
Code de champ modifié ... [23]
Code de champ modifié ... [24]
Code de champ modifié ... [25]
Code de champ modifié ... [26]
Code de champ modifié ... [27]
Code de champ modifié ... [28]
Code de champ modifié ... [29]
Code de champ modifié ... [30]
Code de champ modifié ... [31]
Code de champ modifié ... [32]
Code de champ modifié ... [33]
Code de champ modifié ... [34]
Code de champ modifié ... [35]
Code de champ modifié ... [36]
Code de champ modifié ... [37]
Code de champ modifié ... [38]
Code de champ modifié ... [39]
Code de champ modifié ... [40]
Code de champ modifié ... [41]
Code de champ modifié ... [42]
Code de champ modifié ... [43]
Code de champ modifié ... [44]
Code de champ modifié ... [45]
Code de champ modifié ... [46]
Code de champ modifié ... [47]
Mis en forme ... [48]

Hong, S.-Y., Noh, Y., and Dudhia, J.: A new vertical diffusion package with an explicit treatment of entrainment processes, Mon. Weather Rev., 134, 2318–2341, 2006.

Huang, J., ~~C.~~ Zhang, C., and ~~J. M.~~ Prospero, J. M.~~, 2009~~: Large-scale effect of aerosols on precipitation in the West African Monsoon region Q. J. R. Meteorol. Soc., 135, 581–594, doi:10.1002/qj.391, 2009.

Jaffe, D. A., and Wigder, N. L.: Ozone production from wildfires: A critical review, Atmos. Env., 51, 1-10, 2012.

Kalthoff, N., Lohou, F., Brooks, B., Jegede, G., Adler, B., Babić, K., Dione, C., Ajao, A., Amekudzi, L. K., Aryee, J. N. A., Ayoola, M., Bessardon, G., Danuor, S. K., Handwerker, J., Kohler, M., Lothon, M., Pedruzo-Bagazgoitia, X., Smith, V., Sunmonu, L., Wieser, A., Fink, A. H., and Knippertz, P.: An overview of the diurnal cycle of the atmospheric boundary layer during the West African monsoon season: Results from the 2016 observational campaign, accepted in Atmos. Chem. Phys., https://doi.org/10.5194/acp-2017-631, 2018.

Kim, P. S., Jacob, D. J., Liu, X., Warner, J. X., Yang, K., Chance, K., Thouret, V., and Nedelec, P.: Global ozone–CO correlations from OMI and AIRS: constraints on tropospheric ozone sources, Atmos. Chem. Phys., 13, 9321–9335, 2013.

King, M. D., ~~Y. J.~~ Kaufman, Y. J., ~~W. P.~~ Menzel, W. P., and ~~D.~~ Tanré, D.: Remote-sensing of cloud, aerosol, and water-vapor properties from the Moderate Resolution

Mis en forme : Retrait : Gauche : 0 cm, Suspendu : 0,75 cm, Interligne : Double

Mis en forme : Retrait : Gauche : 0 cm, Suspendu : 0,75 cm, Éviter veuves et orphelines

Mis en forme : Police :Non Italique

Mis en forme : Police :Non Italique

Mis en forme : Police :Non Italique

Imaging Spectrometer (MODIS), IEEE Trans. Geosci. Remote Sens., 30(1), 2–27, 1992.

~~Kalthoff, N., Lohou, F., Brooks, B., Jegede, G., Adler, B., Babić, K., Dione, C., Ajao, A., Amekudzi, L. K., Aryee, J. N. A., Ayoola, M., Bessardon, G., Danuor, S. K., Handwerker, J., Kohler, M., Lothon, M., Pedruzo-Bagazgoitia, X., Smith, V., Sunmonu, L., Wieser, A., Fink, A. H., and Knippertz, P., 2018: An overview of the diurnal cycle of the atmospheric boundary layer during the West African monsoon season: Results from the 2016 observational campaign, accepted in Atmos. Chem. Phys., https://doi.org/10.5194/acp-2017-631~~

Kirchstetter, T. W., Novakov, T., Hobbs, P.V.:, Evidence that the spectral dependence of light absorption by aerosols is affected by organic carbon. J. Geophys. Res. 109, D21208.doi:10.1029/2004JD004999, 2004.

Knippertz, P., ~~A. H.~~ Fink, A. H., ~~A.~~ Deroubaix, A., ~~E.~~ Morris, E., ~~F.~~ Tocquer, F., ~~M.~~ Evans, M., ~~C.~~ Flamant, C., ~~M.~~ Gaetani, M., ~~C.~~ Lavaysse, C., ~~C.~~ Mari, C., ~~J. H.~~ Marsham, J. H., ~~R.~~ Meynadier, R., ~~A.~~ Affo-Dogo, A., ~~T.~~ Bahaga, T., ~~F.~~ Brosse, F., ~~K.~~ Deetz, K., ~~R.~~ Guebsi, R., ~~I.~~ Latifou, I., ~~M.~~ Maranan, M., ~~P. D.~~ Rosenberg, P. D., and ~~A.~~ Schlueter, A. ~~2017~~: A meteorological and chemical overview of the DACCIWA field campaign in West Africa in June–July 2016, *Atmos. Chem. Phys. Disc.*, doi:10.5194/acp-2017-345, 2017.

Knippertz, P., ~~M.~~ Evans, M., ~~P. R.~~ Field, P. R., ~~A. H.~~ Fink, A. H., ~~C.~~ Liousse, C., and ~~J. H.~~ Marsham, J. H.~~, 2015a~~: The possible role of local air pollution in climate change in West Africa. *Nature Clim. Change*, doi:10.1038/NCLIMATE2727, 2015a.

Mis en forme : Allemand (Allemagne)

Mis en forme : Retrait : Gauche : 0 cm, Suspendu : 0,85 cm, Interligne : Double

Mis en forme : Allemand (Allemagne)

Mis en forme : Anglais (États Unis)

Mis en forme : Anglais (États Unis)

Knippertz P., ~~H.~~ Coe, H., ~~C.~~ Chiu, C., ~~M. J.~~ Evans, M. J., ~~A. H.~~ Fink, A. H., ~~N.~~ Kalthoff, N., ~~C.~~ Liousse, C., ~~C.~~ Mari, C., ~~R.~~ Allan, R., ~~B.~~ Brooks B., ~~S.~~ Danour, S., ~~C.~~ Flamant, C., ~~O. O.~~ Jegede, O. O., ~~F.~~ Lohou, F., and ~~J. H.~~ Marsham, J. H.~~, 2015b~~: The DACCIWA project: Dynamics-aerosol-chemistry-cloud interactions in West Africa, *Bull. Amer. Meteorol. Soc.*, **96,** 1451-1460, 2015b.

Lelieveld J., ~~J. S.~~ Evans, J. S., ~~M.~~ Fnais, M., ~~D.~~ Giannadaki, D., and ~~A.~~ Pozzer, A.~~ 2015~~: The contribution of outdoor air pollution sources to premature mortality on a global scale, *Nature*, 525, 367-371, 2015.

Liousse, C., Assamoi, E., Criqui, E. P., Granier, C., and ~~&~~ Rosset, R.~~, 2014~~: Explosive growth in African combustion emissions from 2005 to 2030. *Environ. Res. Lett.* **9,** 035003, 2014.

Lothon M., Said F., Lohou F., and Campistron, B.~~ 2008.~~: Observation of the diurnal cycle in the low troposphere of West Africa. *Mon. Weather Rev.* **136**: 3477–3500, 2008.

Mailler S., ~~L.~~ Menut, L., ~~A. G.~~ Di Sarra, A. G., ~~S.~~ Becagli, S., ~~T.~~ Di Iorio, T., ~~B.~~ Bessagnet, B., ~~R.~~ Briant, R., ~~P.~~ Formenti, P., ~~J.F.~~ Doussin, J.-F., ~~J. L.~~ Gomez-Amo, J. L., ~~M.~~ Mallet, M., ~~G.~~ Rea, G., ~~G.~~ Siour, G., ~~D. M.~~ Sferlazzo, D. M., ~~R.~~ Traversi, R., ~~R.~~ Udisti, R. and ~~S.~~ Turquety, S.~~ 2016~~: On the radiative impact of aerosols on photolysis rates: comparison of simulations and observations in the Lampedusa island during the CharMEx/ADRIMED campaign, Atmos. Chem. Phys., 16, 1219-1244, doi:10.5194/acp-16-1219-2016, 2016.

Mis en forme : Français (France)

Mailler S., ~~L.~~ Menut, L., ~~D.~~ Khvorostyanov, D., ~~M.~~ Valari, M., ~~F.~~ Couvidat, F., ~~G.~~ Siour, G., ~~S.~~ Turquety, S., ~~R.~~ Briant, R., ~~P.~~ Tuccella, P., ~~B.~~ Bessagnet, B., ~~A.~~ Colette, A., ~~L.~~ Letinois, M., and ~~F.~~ Meleux, F.~~2017~~: CHIMERE-2017: from urban to hemispheric chemistry-transport modeling~~—~~, Geosci. Model Dev., 10, 2397-2423, doi:10.5194/gmd-10-2397-2017, 2017.

Mlawer, E. J., Taubman, S. J., Brown, P. D., Iacono, M. J., and Clough, S. A.: Radiative transfer for inhomogeneous atmospheres: RRTM, a validated correlated-k model for the longwave, J. Geophys. Res., 102, 16 663, 1997.

~~Paola~~ Massoli, P.~~-~~, ~~Paul L.~~ Kebabian, P. L.~~-~~, ~~Timothy B.~~ Onasch, T. B.~~-~~, ~~Frank B.~~ Hills, F. B., ~~&~~ and ~~Andrew~~ Freedman, A. ~~(2010~~:~~)~~ Aerosol Light Extinction Measurements by Cavity Attenuated Phase Shift (CAPS) Spectroscopy: Laboratory Validation and Field Deployment of a Compact Aerosol Particle Extinction Monitor, Aerosol Science and Technology, 44:6, 428-435, DOI:10.1080/02786821003716599, 2010.

Menut, L., ~~C.~~ Flamant, C., ~~S.~~ Turquety, S., ~~A.~~ Deroubaix, A., ~~P.~~ Chazette, P., and ~~R.~~ Meynadier, ~~2018~~R.: Impact of biomass burning on pollutants surface concentrations in megacities of the Gulf of Guinea, *Atmos. Chem. Phys.*, 18, 2687-2707, ~~accepted~~2018.

Müller, T., Nowak, A., Wiedensohler, A., Sheridan, P., Laborde, M., Covert, D. S., Marinoni, A., Imre, K., Henzing, B., Roger, J.-C., Martins dos Santos, S., Wilhelm, R., Wang, Y.-Q., and de Leeuw, G.~~, 2009~~: Angular Illumination and Truncation of

Mis en forme : Français (France)

Mis en forme : Police :Non Italique

Three Different Integrating Nephelometers: Implications for Empirical, Size-Based Corrections, Aerosol Sci. Tech., 43(43), 581–586, 2009.

Müller, T., ~~J. S.~~ Henzing, J. S., ~~G.~~ De Leeuw, G.,~~A.~~ Wiedensohler, A., Alastuey, A., Angelov, H., Bizjak, M., Collaud Coen, M., Engström, J. E., Gruening, C., Hillamo, R., Hoffer, A., Imre, K., Ivanow, P., Jennings, G., Sun, J. Y., Kalivitis, N., Karlsson, H., Komppula, M., Laj, P., Li, S.-M., Lunder, C., Marinoni, A., Martins dos Santos, S., Moerman, M., Nowak, A., Ogren, J. A., Petzold, A., Pichon, J. M., Rodriquez, S., Sharma, S., Sheridan, P. J., Teinilä, K., Tuch, T., Viana, M., Virkkula, A., Weingartner, E., Wilhelm, R., and Wang, Y. Q.~~et al., 2011~~: Characterization and intercomparison of aerosol absorption photometers: result of two intercomparison workshops, Atmos. Meas. Tech., 4, 245-268, 2011.

Parker, D. J., Kassimou, A., Orji, B. N., Osika, D. P., Hamza, I., Diop-Kane, M., Fink, A., Galvin, J., Guichard, F., Lamptey, B. L., Hamidou, H., van der Linden, R., Redl, R., Lebel, T., and Tubbs, C.~~, 2017~~: Local Weather, in Meteorology of Tropical West Africa: The Forecasters' Handbook (eds D. J. Parker and M. Diop-Kane), John Wiley & Sons, Ltd, Chichester, UK. doi: 10.1002/9781118391297.ch4, 2017.

Parker, D. J., Burton, R. R., Diongue-Niang, A., Ellis, R. J., Felton, M. A., Taylor, C.M., Thorncroft, C. D., Bessemoulin, P., and Tompkins, A.~~, 2005~~: The diurnal cycle of the West African Monsoon circulation. *Q. J. R. Meteorol. Soc.* **131**: 2839–2860, 2005.

Remer, L.A., Kaufman, Y.J., Tanré, D., Mattoo, S., Chu, D.A., Martins, J. V., Li, R.-R., Ichoku, C., Levy, R.C., Kleidman, R.G., Eck, T.F., Vermote, E., and Holben, B.N.~~,~~

Mis en forme : Police :Century Gothic, 11 pt, Anglais (États Unis)

Mis en forme : Vérifier l'orthographe et la grammaire

~~2005.~~: The MODIS Aerosol Algorithm, Products, and Validation. J. Atmos. Sci. 62, 947–973. doi:10.1175/JAS3385.1, 2005.

Russell, P. B., Bergstrom, R. W., Shinozuka, Y., Clarke, A. D., DeCarlo, P. F., Jimenez, J. L., Livingston, J. M., Redemann, J., Dubovik, O., and Strawa, A.: Absorption Angstrom Exponent in AERONET and related data as an indicator of aerosol composition, Atmos. Chem. Phys., 10, 1155-1169, https://doi.org/10.5194/acp-10-1155-2010, 2010.

Shamarock, W.C., and ~~J.B.~~ Klemp, J. B.~~2008~~: A time-split nonhydrostatic atmospheric model for weather research and forecasting applications, Journal of Computational Physics 227 (2008) 3465–3485, 2008.

Shang, X., and Chazette, P. ~~(2014).~~: Interest of a Full-Waveform Flown UV Lidar to Derive Forest Vertical Structures and Aboveground Carbon, Forests, 5, 1454-1480; doi:10.3390/f5061454, 2014.

Spicer, C. W., Joseph, D. W., and Ollison, W. M.: A Re-Examination of Ambient Air Ozone Monitor Interferences, J. Air & Waste Manage. Assoc. **60**:1353–1364, 2010.

Thiébaux, J., ~~E.~~ Rogers, E., ~~W.~~ Wang, E., and ~~B.~~ Katz, B., ~~2003~~: A new high-resolution blended real-time global sea surface temperature analysis, Bull. Amer. Meteorol. Soc., 84, 645-656, doi:10.1175/BAMS-84-5-645, 2003.

Toledano, C. , Cachorro, V. E., Berjon, A. , de Frutos, A. M., Sorribas, M. , de la Morena, B. A. and Goloub, P.: Aerosol optical depth and Ångström exponent

Mis en forme : Anglais (États Unis)

Mis en forme : Anglais (États Unis)

Mis en forme : Retrait : Gauche : 0 cm, Suspendu : 0,75 cm, Interligne : Double

Mis en forme : Anglais (États Unis)

climatology at El Arenosillo AERONET site (Huelva, Spain). Q.J.R. Meteorol. Soc., 133: 795-807. doi:10.1002/qj.54, 2007.

Werdell, P.J., ~~B.A.~~ Franz, B. A., ~~S.W.~~ Bailey, S. W., ~~G.C.~~ Feldman, G. C., and 15 co-authors~~, 2013~~: Generalized ocean color inversion model for retrieving marine inherent optical properties, Applied Optics 52, 2019-2037, 2013.

Winker, D. M., ~~W. H.~~ Hunt, W. H., and ~~M. J.~~ McGill, M. J.: ~~(2007),~~ Initial performance assessment of CALIOP, Geophys. Res. Lett., 34(19), doi:10.1029/2007GL030135, 2007.

World Urbanization Prospects: The 2014 Revision, United Nations, Department of Economic and Social Affairs, Population Division, 2015, ST/ESA/SER.A/366, Pp 517, http://www.un.org/en/development/desa/population/publications/pdf/urbanization/WUP2011_Report.pdf

Zhang, Y., ~~R.~~ Fu, R., ~~H.~~ Yu, H., ~~R. E.~~ Dickinson, R. E., ~~R. N.~~ Juarez, R. N., ~~M.~~ Chin, M., and H. Wang, H.~~2008~~: A regional climate model study of how biomass burning aerosol impacts land-atmosphere interactions over the Amazon, J. Geophys. Res., 113, D14S15, doi:10.1029/2007JD009449, 2008.

Zhang, Y., ~~R.~~ Fu, R., ~~H.~~ Yu, H., ~~Y.~~ Qian, Y., ~~R.~~ Dickinson, R., ~~M. A. F.~~ Silva Dias, M. A. F., ~~P. L.~~ da Silva Dias, P. L., and K. Fernandes, K. ~~2009~~: Impact of biomass burning aerosol on the monsoon circulation transition over Amazonia, Geophys. Res. Lett., 36, *L10814*, *doi:*10.1029/2009GL037180, 2009.

Mis en forme : Anglais (États Unis)

Mis en forme : Français (France)

Mis en forme : Français (France)

Mis en forme : Français (France)

Mis en forme : Français (France)

Mis en forme : Français (France)

Mis en forme : Français (France)

Mis en forme : Français (France)

Code de champ modifié

1286 **Tables**

1287

1288 Table 1. SAFIRE ATR 42 payload. Only instruments used in this study are listed. The

1289 complete payload is detailed in the Supplementary Material of Flamant et al. (2018).

Instrument	Parameter	Responsible institution
P (static & dynamic): Rosemount 120 & 1221	Pressure 1 s time resolution	SAFIRE / CNRS
INS + GPS inertial units	Wind component, position 1 s time resolution	SAFIRE / CNRS
Adjustable (flow, orientation) Aerosol Community Inlet	Particle aerosol sampling D50 = 5 µm	CNRM / CNRS
Aircraft DUAL CPC counter MARIE	Particle number concentrations D>4 nm & D>15 nm (variable) 1 s time resolution Uncertainty: 10%	LaMP / UBP
OPC Grimm 1.109	Ambient particle size distribution 0.25–25 µm 6 s time resolution	CNRM / CNRS
PSAP (3λ)	Absorption coefficient, black carbon content Blue 476 nm, green 530 nm, red 660 nm 10 s time resolution Uncertainty: 30%	LaMP / UPB
CAPS-PMex	Extinction Mm^{-1} at 530 nm 1 s time resolution Uncertainty: 3%	CNRM / CNRS

TEI 49i	O_3 20 s time resolution Precision: 1 ppbv	SAFIRE / CNRS
TEI 42CTL NOx analyser	NOx 8 s time resolution Precision: 50 ppt integration over 120 s	SAFIRE / CNRS
PICARRO	CO cavity ring down spectroscopy 5 s time resolution Precision: 30 ppb	SAFIRE / CNRS
ULICE Aerosol / cloud lidar	Aerosol backscatter @ 355 nm Resolution: 15 m on the vertical, averaged over 10 s (1000 shots) on the horizontal.	LSCE / UPMC

Table 2. Correlation between vertical velocity and land-sea skin temperature gradients at 0000, 0600, 1200 and 1800 UTC for July 2016. The land-sea zonal skin temperature gradient is computed using a 'land box' defined as 6–9°E and 4.5–6.5°N and a 'sea box' defined as 2–5°E and 4.5–6.5°N. The land-sea meridional skin temperature gradient is computed using a 'land box' defined as 2°W–2°E and 6–8°N and a 'sea box' defined as 2°W–2°E and 3–5°N. Vertical velocity is averaged in the layer 850–600 hPa over a box defined as 2°W–2°E and 4–6°N. Correlations are computed using vertical velocity and skin temperature gradient indices standardized to 0000, 0600, 1200 and 1800 UTC means for the month of July 2016. Significant correlations (and their p values) are given in bold.

Zonal cell		Vertical velocity			
		0000 UTC	0600 UTC	1200 UTC	1800 UTC
Skin temperature gradient	0000 UTC	0.26	-0.04	0.12	-0.17
	0600 UTC		-0.08	0.09	0.11
	1200 UTC			0.02	**0.53 (p=0.002)**
	1800 UTC				**0.46 (p=0.01)**
Meridional cell		**Vertical velocity**			
		0000 UTC	0600 UTC	1200 UTC	1800 UTC
Skin temperature gradient	0000 UTC	0.07	-0.22	0.06	-0.07
	0600 UTC		-0.01	0.01	-0.06
	1200 UTC			**0.34 (p=0.06)**	-0.24

	1800 UTC				0.20

1305

1306 **Figures**

1307

(a)

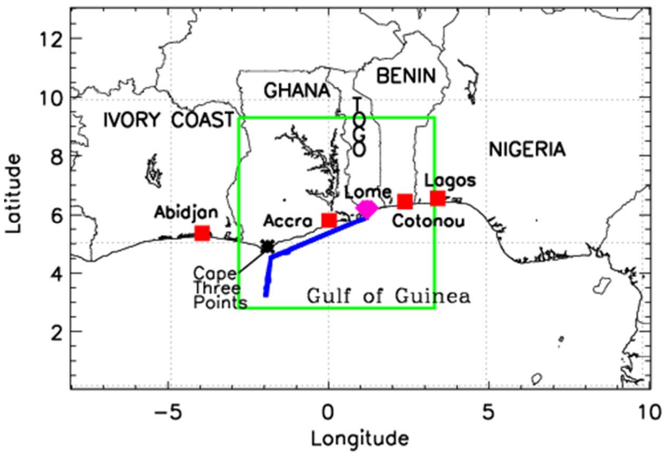

(b)

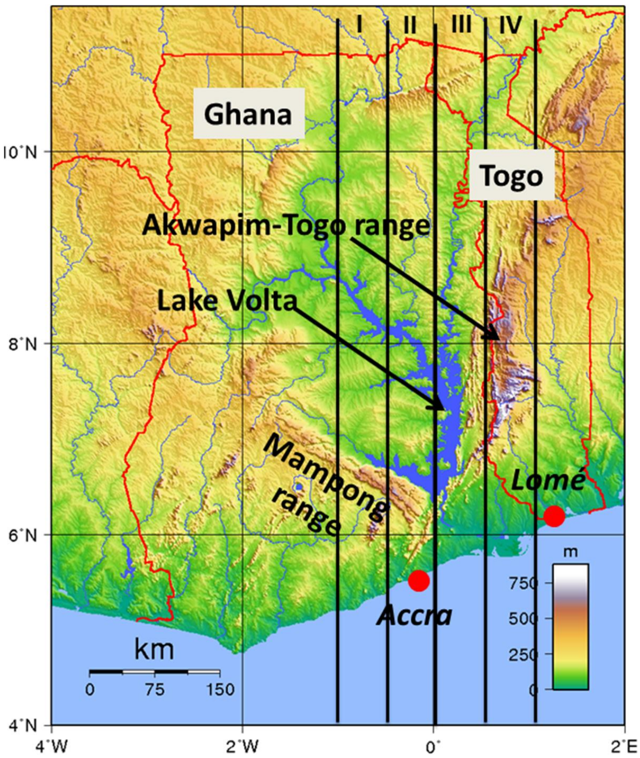

Figure 1: (a) Map of southern West Africa with the location of the main landmarks (e.g. cities, countries). The thick blue line represents the ATR 42 flight track in the afternoon of 2 July 2016. The red filled square symbols represent DACCIWA radiosounding stations used in this study. The pink filled circle represents the base of operation for aircraft during the DACCIWA field campaign. The green thick box represents the domain of the 2-km WRF simulation. (b) Topographic map of Ghana and Togo showing the main features of interest for this study as well as the transects along which tracer simulations are shown in **Figure 8**. The transects are centered at 0.75°W, 0.25°W, 0.25°E and 0.75°E (for I, II, III and IV, respectively) and are 0.5° wide.

(a)

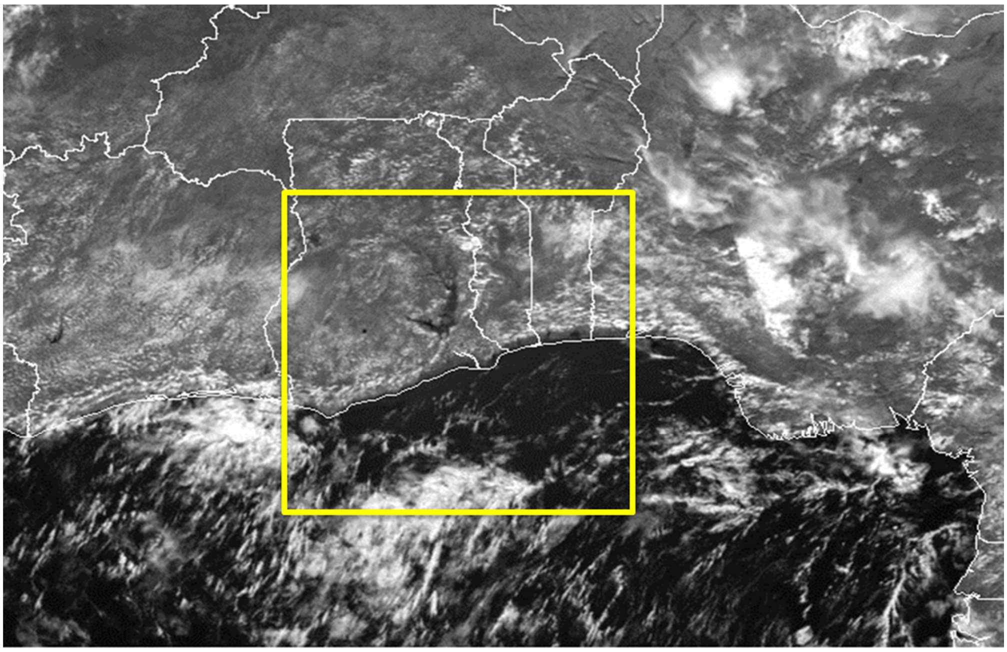

(b)

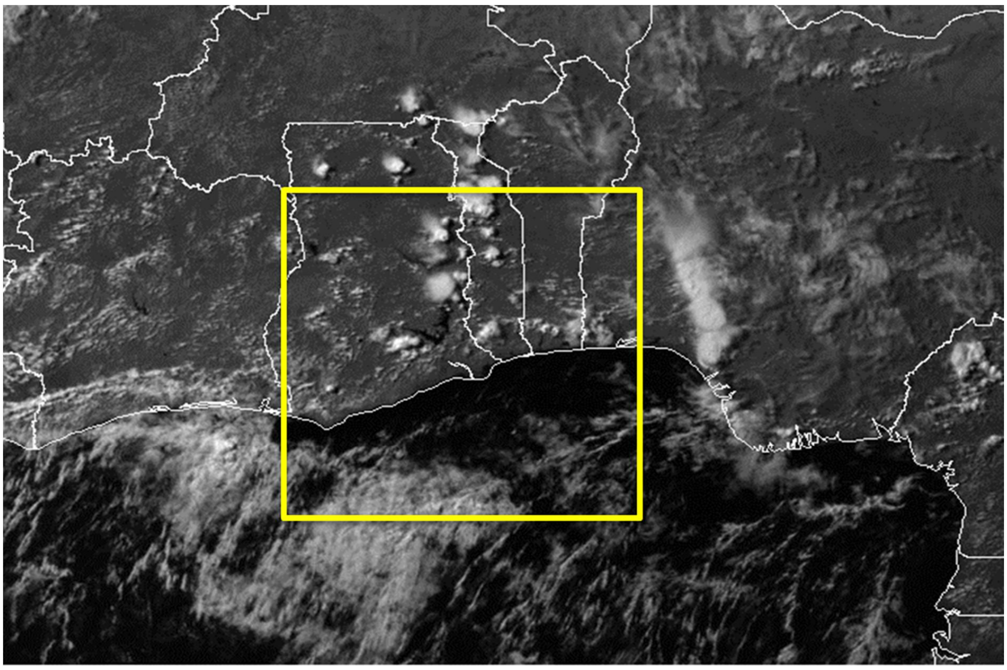

Figure 2: SEVIRI visible images of SWA on 2 July at (a) 1200 UTC and (b) 1500 UTC. Country borders are shown as solid white lines. The yellow thick box represents the domain of the 2-km WRF simulation as in **Figure 1a**. The coordinates of the lower left corner of the images are 0°N/8°W, and the coordinates of the upper right corner of the images are 13°N/10°45'E.

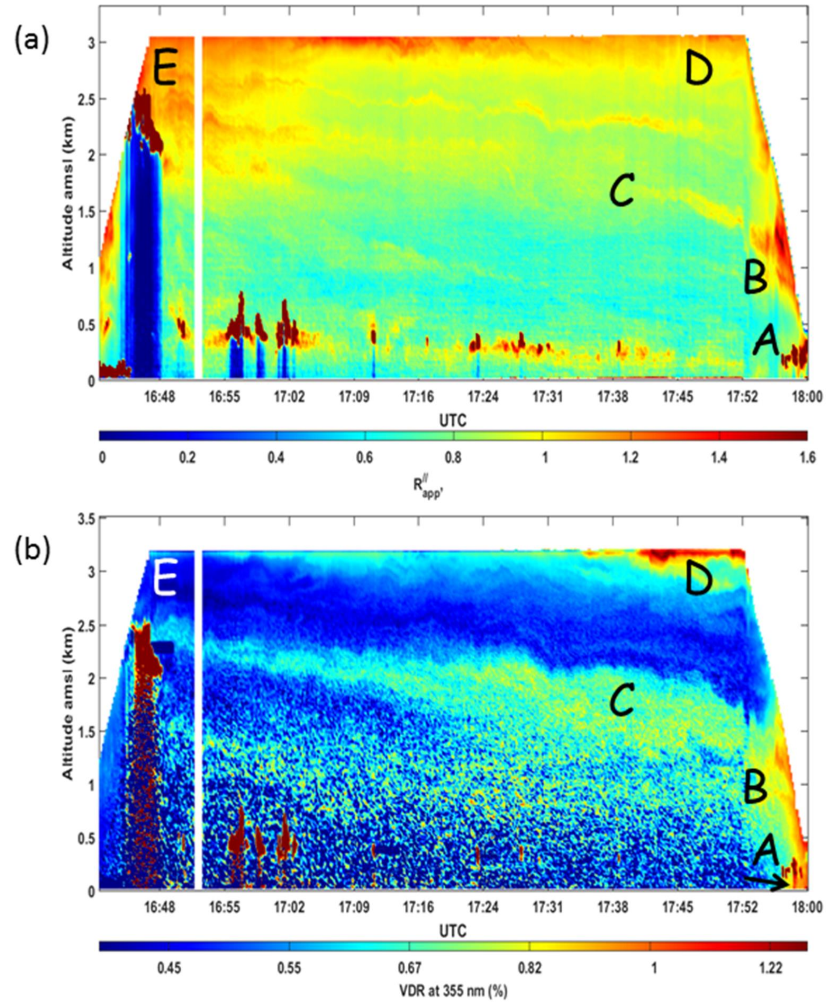

Figure 3: Time-height evolution of ULICE-derived (a) apparent scattering ratio (R_{app}) and (b) volume depolarization ratio (VDR) below the ATR 42 flight track over the Gulf of Guinea between 1644 and 1800 UTC on 2 July 2016 (see **Figure 1a**). The ATR leg parallel to the coastline starts at 1654 UTC. The ATR passed the longitude of Accra at 1729 UTC. See text for explanations of features A–E. The arrow in (b) points to feature A. The distance covered by the ATR 42 along this transect is ~450 km.

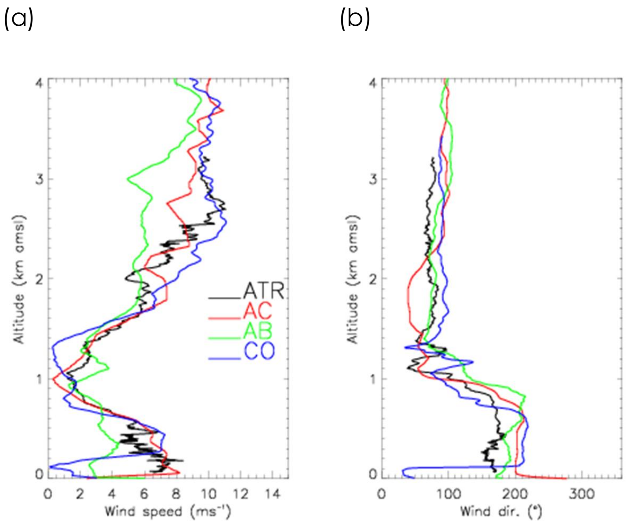

Figure 4: (a) Wind speed and (b) wind direction profiles measured during the ATR 42 sounding over the ocean (1630 to 1647 UTC, ATR, black solid line) as well as from the radiosoundings launched in Accra at 1700 UTC (AC, red solid line), in Abidjan at 1608 UTC (AB, green solid line) and in Cotonou at 1612 UTC (CO, blue solid line). The location of the radiosounding sites is shown in **Figure 1a**.

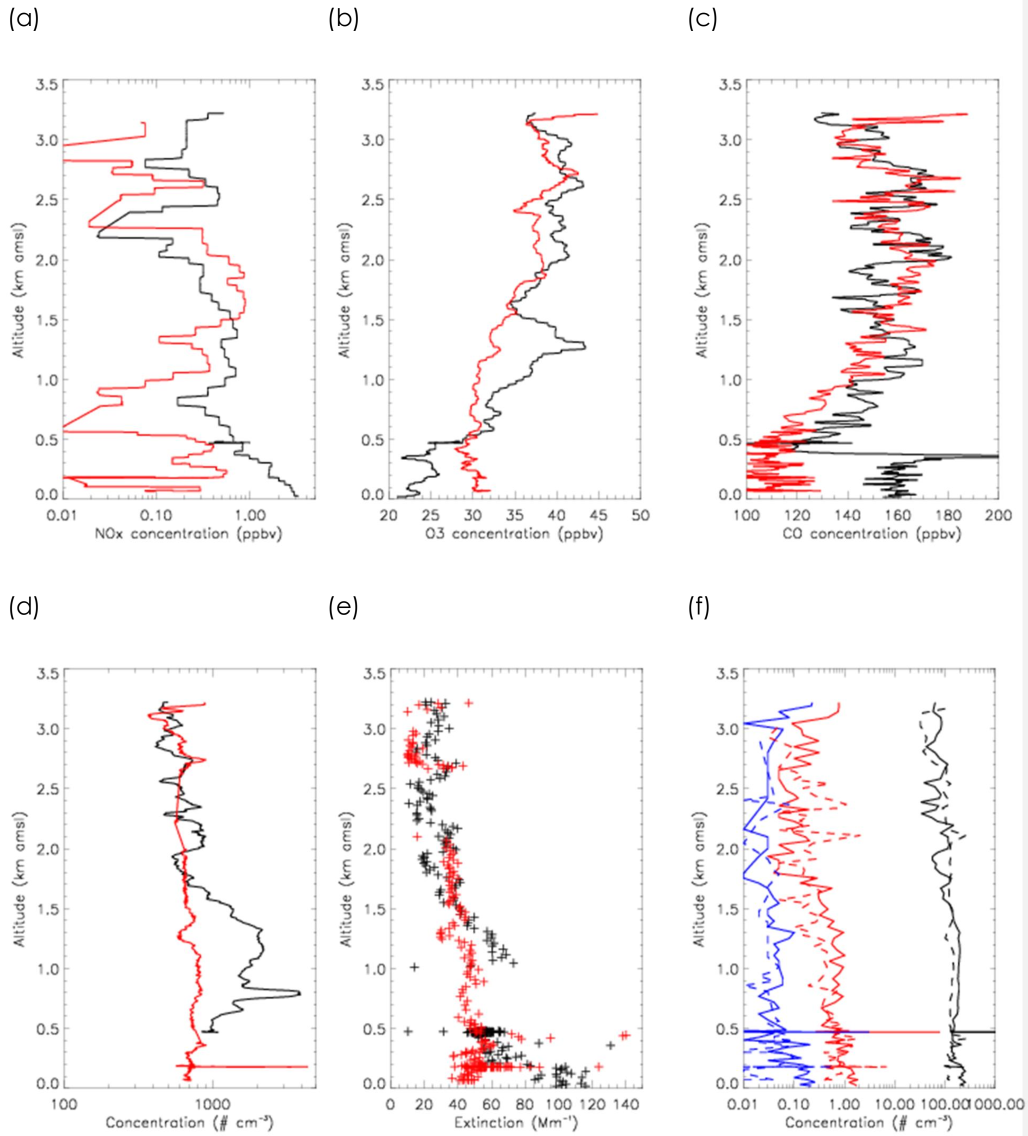
(a)
(b)
(c)
(d)
(e)
(f)
Altitude (km amsl)
0.0 0.5 1.0 1.5 2.0 2.5 3.0 3.5
0.01 0.10 1.00
NOx concentration (ppbv)
20 25 30 35 40 45 50
O3 concentration (ppbv)
100 120 140 160 180 200
CO concentration (ppbv)
100 1000
Concentration (# cm⁻³)
0 20 40 60 80 100 120 140
Extinction (Mm⁻¹)
0.01 0.10 1.00 10.00 100.00 1000.00
Concentration (# cm⁻³)

(g)

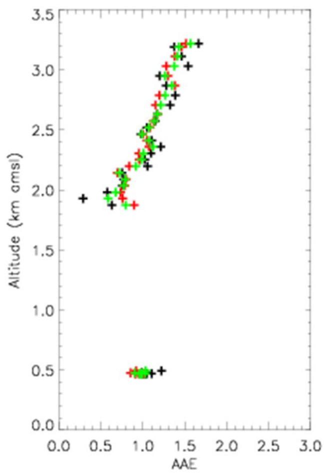

Figure 5: Profiles measured during the ATR 42 sounding over the ocean (1633 to 1647 UTC, red solid line) and at the coast in the vicinity of Lomé (1753 to 1807 UTC, black solid line) for (a) NO_x concentration, (b) O_3 concentration, (c) CO concentration, (d) total aerosol concentration N_{10} measured with the CPC and (e) extinction coefficient. (f) N_{PM1}, $N_{PM2.5}$ and N_{PM10} concentration profiles (black, red and blue, respectively) measured over the ocean (dashed lines) and at the coast in the vicinity of Lomé (solid lines). (g) AAE profiles in the vicinity of Lomé computed between 467 and 530 nm, 530 and 660 nm, and 467 and 660 nm (black, red and green solid symbols, respectively).

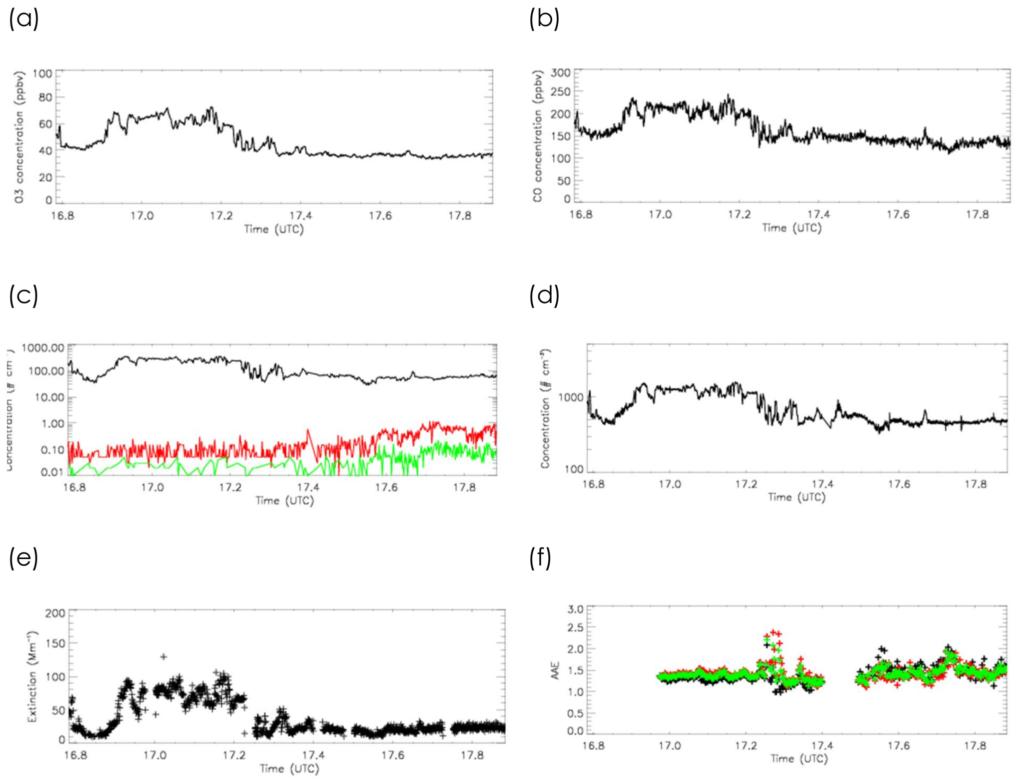

Figure 6: (a) O_3 concentration, (b) CO concentration, (c) N_{PM1}, $N_{PM2.5}$ and N_{PM10} concentrations (black, red and green, respectively), (d) CPC-derived total aerosol concentration N_{10}, (e) extinction coefficient and (f) AAE computed between 476 and 530 nm, 530 and 660 nm, and 476 and 660 nm (black, red and green crosses, respectively) measured during the ATR 42 elevated straight level run from 1647 to 1753 UTC. The distance covered by the ATR 42 along this transect is ~395 km.

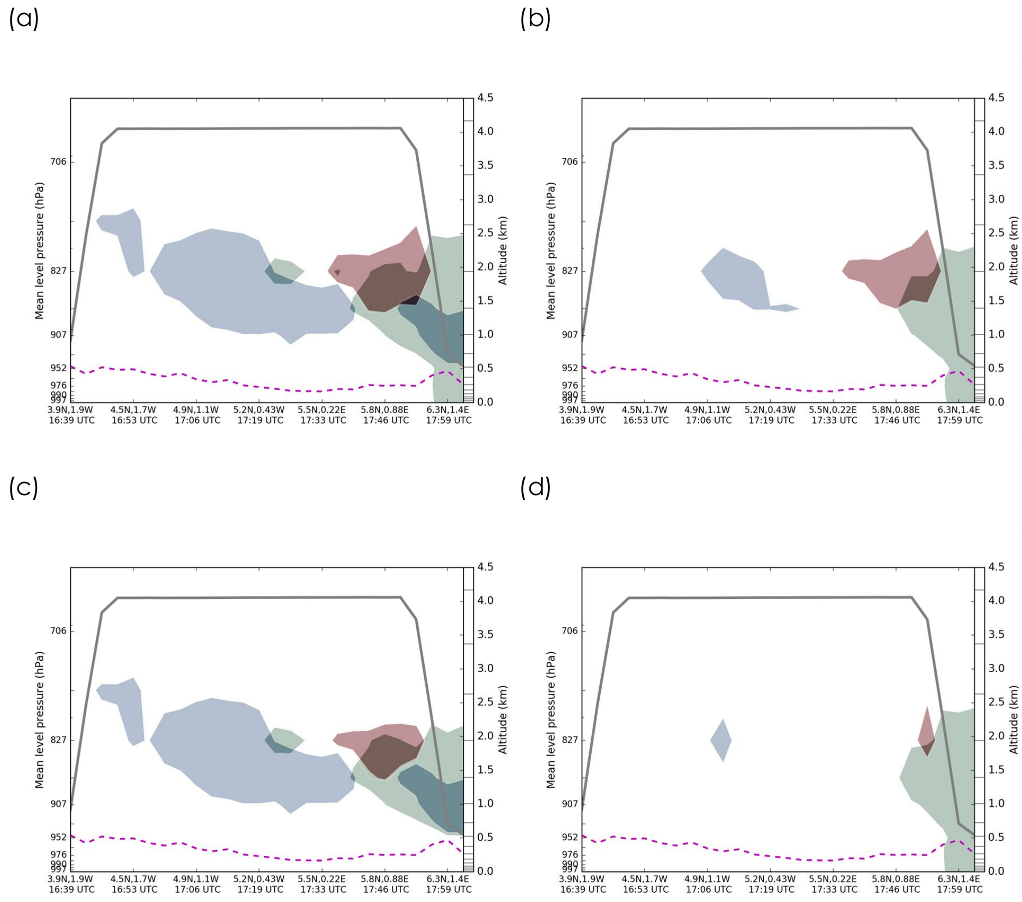

Figure 7: Time-height evolution of tracer concentration (a.u.) below the ATR 42 between 1400 and 1800 UTC for (a) the TRA_D12, (b) TRA_I12, (c) TRA_D1~~2~~ and (d) TRA_D2~~3~~ experiments (see section 3.2.1 for details). Tracer emissions in Accra, Lomé and Cotonou appear in blueish, greenish and reddish colors, respectively. The solid grey line represents the altitude of the aircraft. The dashed ~~blue~~ magenta line represents the height of the top of the marine ABL from the WRF 2-km simulation.

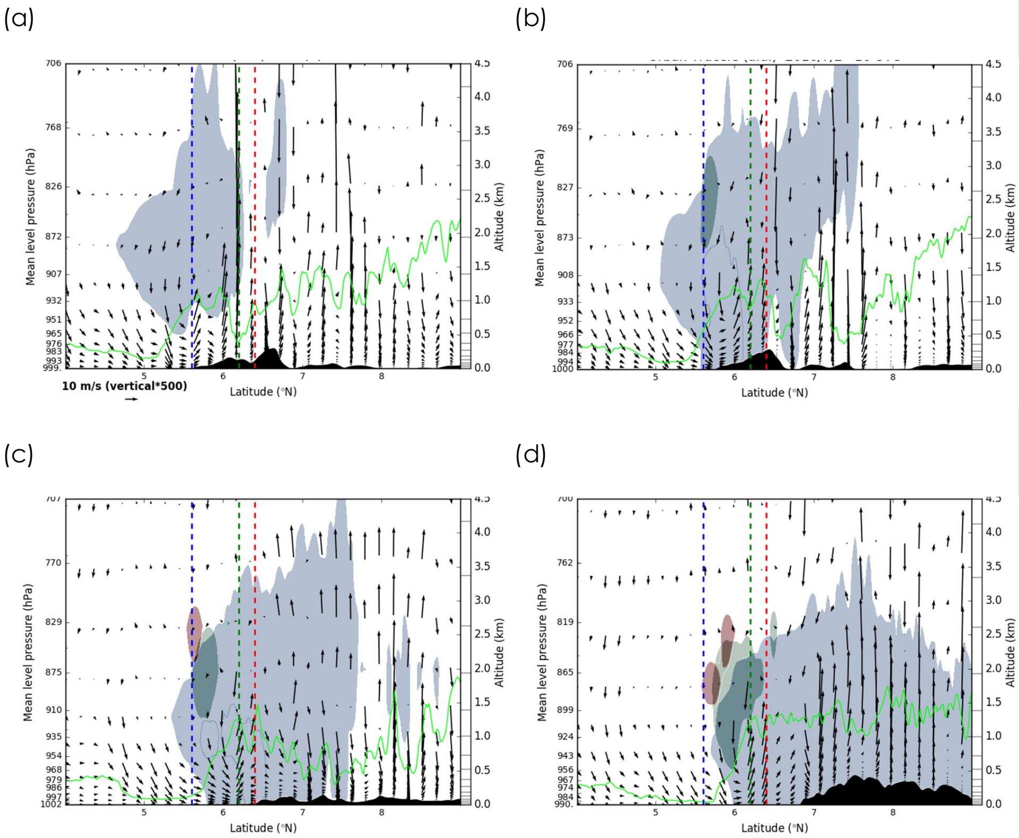

Figure 8: Tracer concentrations (a.u.) from the TRA_D12 experiment (see section 3.2.1 for details) along four 0.5°-wide north–south transects centered on (a) 0.75°W, (b) 0.25°W, (c) 0.25°E and (d) 0.75°E (marked I, II, III and IV, respectively, in **Figure 1b**) at 1600 UTC. Tracer emissions in Accra, Lomé and Cotonou appear in blueish, greenish and reddish colors, respectively, as in **Figure 7**. Also shown are meridional-vertical wind vectors in the transects. The green solid line represents the ABL derived from the WRF 2-km simulation. The vertical dashed lines represent the location of the cities of Accra (blue), Lomé (green) and Cotonou (red). The orography along the transects is shaded in black.

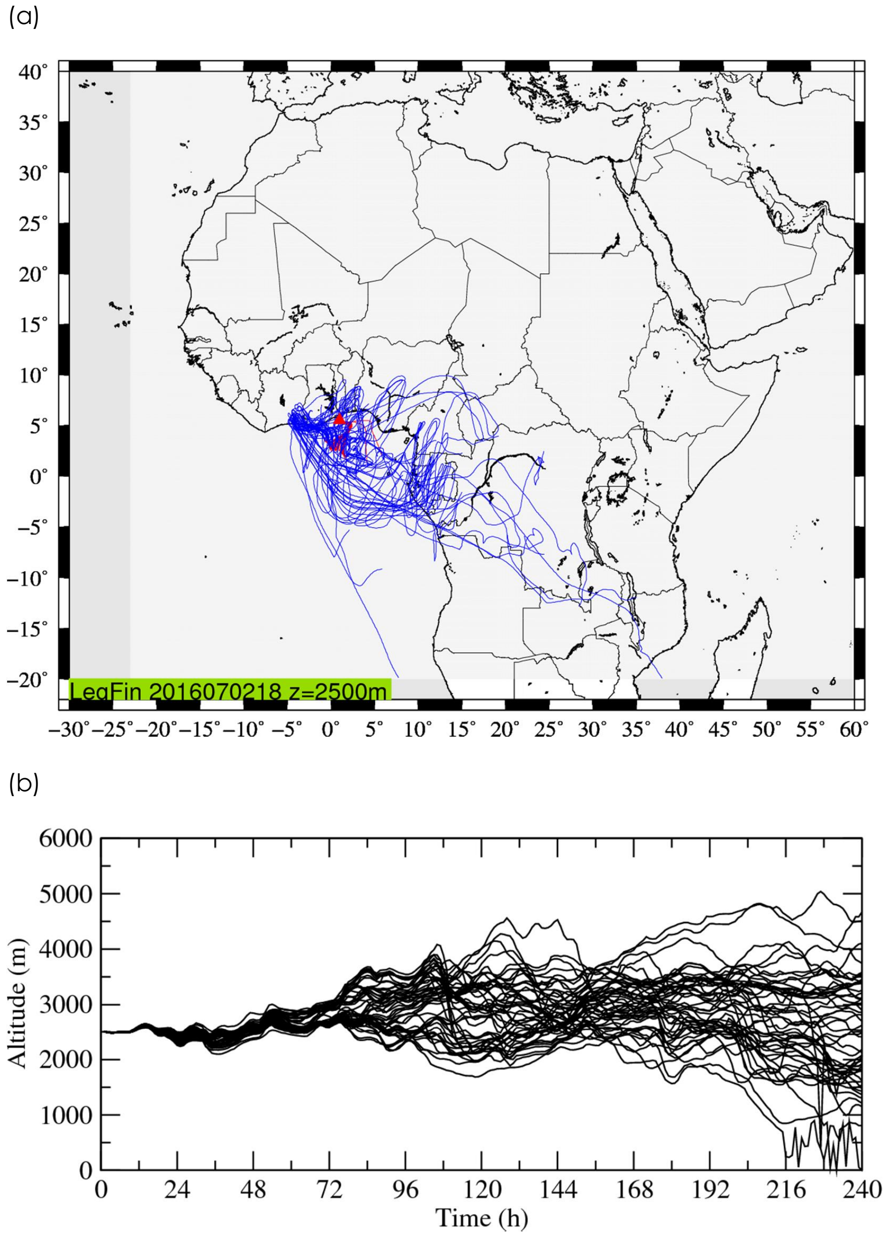

Figure 9: 10-day CHIMERE-derived backplume ending at 2500 m amsl at 5.5°N/1°E at 1700 UTC on 2 July 2016. (a) Individual trajectories are shown as blue solid lines over a political map of Africa with state borders appearing in black. The red triangle

indicates the location of the origin of the back trajectories. (b) Time-height representation of the individual back trajectories shown in the top panel.

(a)

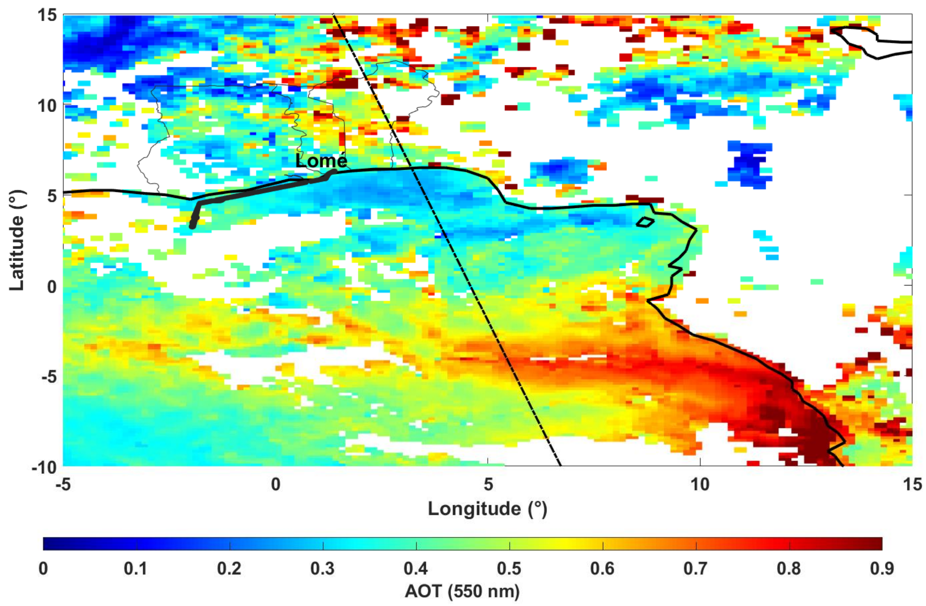

(b)

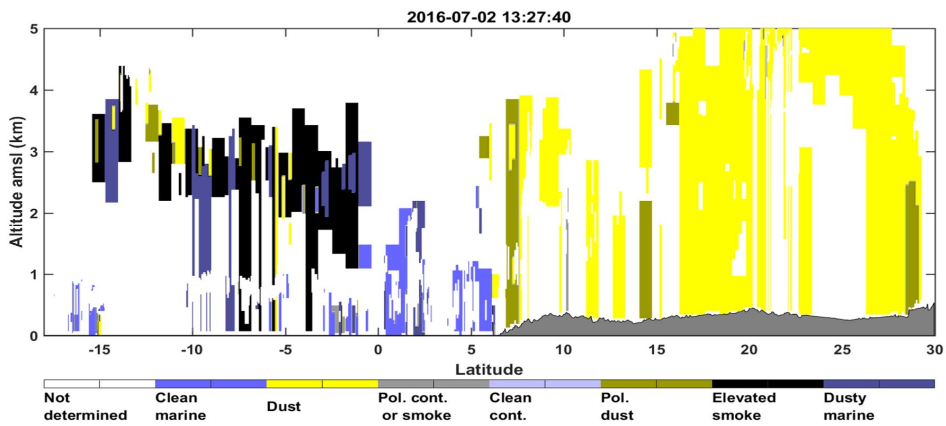

Figure 10: (a) Daily AOD obtained by averaging MODIS Dark target AOD (at 1325 UTC) and SEVIRI AOD (daily mean) on 2 July 2016. White areas indicate missing data. Country borders of Ghana, Togo and Benin are shown as thin solid black lines. The straight dashed-dotted line indicates the location of the CALIOP afternoon overpass

at 1327 UTC. The thick solid black line represents the ATR 42 flight track. (b) CALIOP-derived aerosol classification for the afternoon overpass.

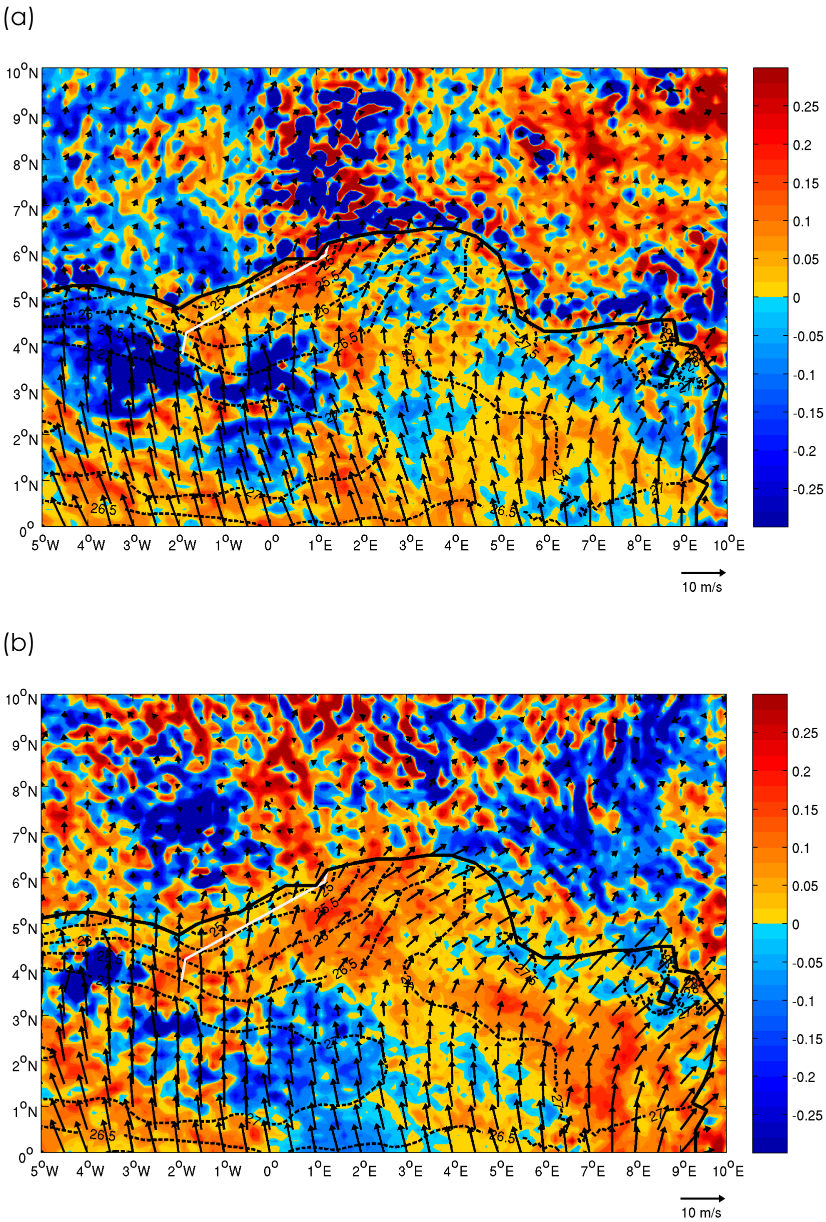

Figure 11: Vertical velocity averaged between 850 and 600 hPa (color, Pa s^{-1}) with 10-m winds (vectors) and SST (contours, black dotted lines) from IFS analyses at (a)

1200 UTC and (b) 1800 UTC. The thick black line represents the SWA coastline. The straight white line represents the ATR 42 flight track.

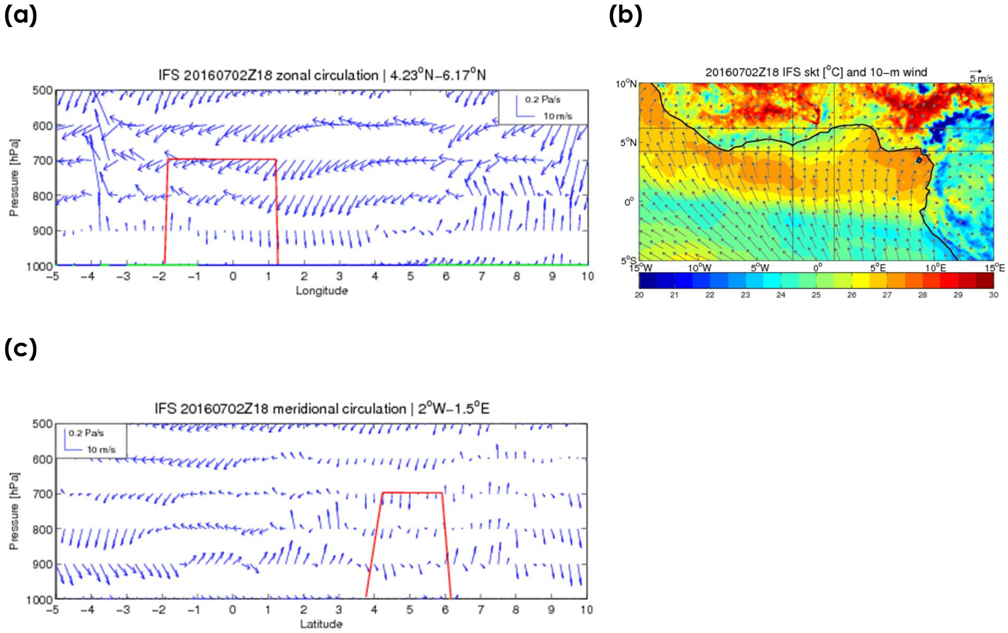

Figure 12: (a) West–east oriented vertical cross section (1000–500 hPa) of zonal-vertical wind vectors from IFS analyses (blue) between 5°W and 10°E averaged between 4.54°N and 6.17°N at 1800 UTC on 2 July 2016. The thick red line is the projection of the ATR 42 aircraft track onto the cross-section. The thick green and blue lines at the bottom of the graph indicate the presence of land and ocean, respectively. Surface characteristics are defined based on the dominating surface type in the latitudinal band considered for the average of the wind field. (b) IFS skin temperature (colors) and wind field at 10 m (vectors) at 1800 UTC. The former, originally at 0.125° resolution, has been linearly interpolated onto the Copernicus grid at 5 km before computing the skin temperature differences between the observations and the model. (c) North-south oriented vertical cross section (1000–500 hPa) of meridional-vertical wind vectors from IFS analyses (blue) between 5°S and 10°N averaged between 2°W and 1.5°E at 1800 UTC. The thick red line is the

projection of the ATR 42 aircraft track onto the cross-section. Cross-sections shown in (a) and (c) are computed in the zonal and meridian windows delimited east-west and north-south lines, respectively, shown in (b).

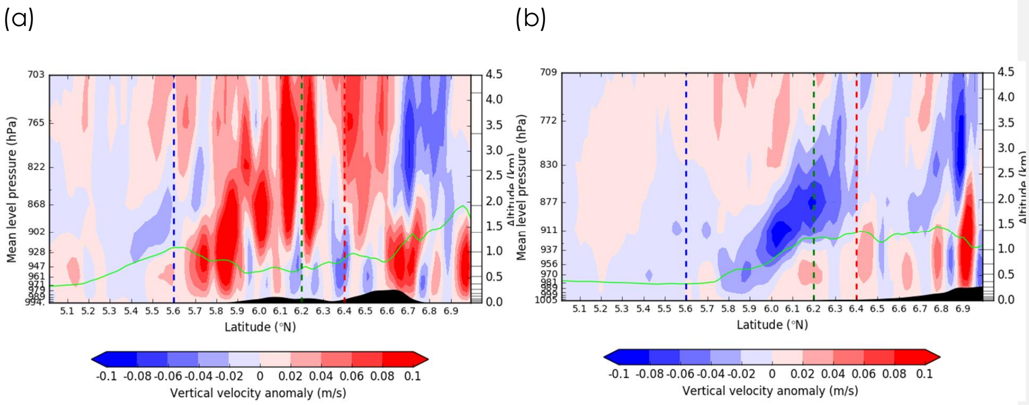

Figure 13: Vertical velocity anomaly along (a) the western most transect shown in Figure 1b (transect I) and (b) the eastern most transect shown in Figure 1b (transect IV), from the WRF 2-km simulation. The anomalies are computed with respect to the average vertical velocity between 1°W and 1°E.

Page 44 : [1] Modifier	Unknown

Code de champ modifié

Page 44 : [2] Modifier	Unknown

Code de champ modifié

Page 44 : [3] Modifier	Unknown

Code de champ modifié

Page 44 : [4] Modifier	Unknown

Code de champ modifié

Page 44 : [5] Modifier	Unknown

Code de champ modifié

Page 44 : [6] Modifier	Unknown

Code de champ modifié

Page 44 : [7] Modifier	Unknown

Code de champ modifié

Page 44 : [8] Modifier	Unknown

Code de champ modifié

Page 44 : [9] Modifier	Unknown

Code de champ modifié

Page 44 : [10] Modifier	Unknown

Code de champ modifié

Page 44 : [11] Modifier	Unknown

Code de champ modifié

Page 44 : [12] Modifier	Unknown

Code de champ modifié

Page 44 : [13] Modifier	Unknown

Code de champ modifié

Page 44 : [14] Modifier	Unknown

Code de champ modifié

Page 44 : [15] Modifier	Unknown

Code de champ modifié

Page 44 : [16] Modifier	Unknown

Code de champ modifié

Page 44 : [17] Modifier	Unknown

Code de champ modifié

Page 44 : [18] Modifier	Unknown

Code de champ modifié

Page 44 : [19] Modifier	Unknown

Code de champ modifié

Page 44 : [20] Modifier	Unknown

Code de champ modifié

Page 44 : [21] Modifier	Unknown

Code de champ modifié

Page 44 : [22] Modifier	Unknown

Code de champ modifié

Page 44 : [23] Modifier	Unknown

Code de champ modifié

Page 44 : [24] Modifier	Unknown

Code de champ modifié

Page 44 : [25] Modifier	Unknown

Code de champ modifié

Page 44 : [26] Modifier	Unknown

Code de champ modifié

Page 44 : [27] Modifier	Unknown

Code de champ modifié

Page 44 : [28] Modifier	Unknown

Code de champ modifié

Page 44 : [29] Modifier	Unknown

Code de champ modifié

Page 44 : [30] Modifier	Unknown

Code de champ modifié

Page 44 : [31] Modifier	Unknown

Code de champ modifié

Page 44 : [32] Modifier	Unknown

Code de champ modifié

Page 44 : [33] Modifier	Unknown

Code de champ modifié

Page 44 : [34] Modifier	Unknown

Code de champ modifié

Page 44 : [35] Modifier	Unknown

Code de champ modifié

Page 44 : [36] Modifier	Unknown

Code de champ modifié

Page 44 : [37] Modifier	Unknown

Code de champ modifié

Page 44 : [38] Modifier	Unknown

Code de champ modifié

Page 44 : [39] Modifier	Unknown

Code de champ modifié

Page 44 : [40] Modifier	Unknown

Code de champ modifié

Page 44 : [41] Modifier	**Unknown**	

Code de champ modifié

Page 44 : [42] Modifier	**Unknown**	

Code de champ modifié

Page 44 : [43] Modifier	**Unknown**	

Code de champ modifié

Page 44 : [44] Modifier	**Unknown**	

Code de champ modifié

Page 44 : [45] Modifier	**Unknown**	

Code de champ modifié

Page 44 : [46] Modifier	**Unknown**	

Code de champ modifié

Page 44 : [47] Modifier	**Unknown**	

Code de champ modifié

Page 44 : [48] Mis en forme	**cyf**	**29/06/2018 07:08:00**

Retrait : Gauche : 0 cm, Suspendu : 0,75 cm, Interligne : Double